INDIUM PHOSPHIDE PHOTONIC INTEGRATED CIRCUIT TESTING

by

Keith A. McKinzie Jr.

A Thesis

Submitted to the Faculty of Purdue University

In Partial Fulfillment of the Requirements for the degree of

Master of Science in Electrical and Computer Engineering

School of Electrical and Computer Engineering at Purdue Northwest

West Lafayette, Indiana

August 2021

THE PURDUE UNIVERSITY GRADUATE SCHOOL
STATEMENT OF COMMITTEE APPROVAL

Dr. Andrew Weiner, Chair

School of Electrical and Computer Engineering

Dr. Evgenii Narimanov

School of Electrical and Computer Engineering

Dr. Dana Weinstein

School of Electrical and Computer Engineering

Dr. Peter Bermel

School of Electrical and Computer Engineering

Approved by:

Dr. Dimitrios Peroulis

TABLE OF CONTENTS

LIST OF TABLES 4

LIST OF FIGURES 5

ABSTRACT 6

1 INTRODUCTION 7

2 INP HIGH-POWER WIDELY TUNABLE LASER MONOLITHICALLY INTEGRATED WITH SOA ARRAY 12

2.1 Introduction 12

2.2 Device Structures 12

2.3 Optical Power Testing 14

2.4 Widely Tunable Narrow Linewidth Pump Laser 21

2.4.1 Linewidth Measurement Sensitivity 24

2.4.2 Reported M-MOPA Device Linewidth Across the Extended C-band . 27

2.5 Hybrid Integration of InP High Power Laser and SiN Microresonator 28

3 INP INTEGRATED PULSE SHAPER WITH 48 CHANNEL, 50 GHZ SPACING AMPLITUDE AND PHASE CONTROL 35

3.1 Introduction 35

3.2 Phase Shaping 35

REFERENCES 38

LIST OF TABLES

2.1 InP Laser with SOA Array Power Scaling 20

LIST OF FIGURES

2.1 InP Laser and SOA Configurations 13
2.2 Two SOA Laser Interference and Output Power 15
2.3 InP Laser Quad-SOA Iterative Coherent Combination and Stability 17
2.4 Segmented SOA Output Power vs. Bias 18
2.5 Quad SOA MOPA Interference Scan 20
2.6 InP Master Laser Tuning 21
2.7 InP Laser Tuning, Low and High Power 22
2.8 Modified delayed self-heterodyne setup 25
2.9 Discrete Mode Laser vs. Master Laser 26
2.10 Instrument FM Noise Floor Resolution 27
2.11 Laser's Recorded Output Spectra and Linewidths Across the Extended C-band 28
2.12 Heterogeneous integrated device architecture 30
2.13 Laser assembly 30
2.14 View of bonded microring resonators. 31
2.15 Early iteration hybrid device testing 33
2.16 Hybrid lasing 34
3.1 Loopback AWGPS two-line experiment 35
3.2 AWGPS channel phase shift 36
3.3 E-field cross-correlation time and frequency domain 37
3.4 Phase shaping, start and finish 37

ABSTRACT

Here I report work done to develop an integrated amplitude and phase shaped optical frequency comb as a source for RF photonic signal processing. The first published section of work pushed towards integrated comb generation; in this work, InP devices were provided by Infinera corp., and SiN devices fabricated by professor Minghao Qi's group. In this work a monolithic InP-based photonic integrated circuit (PIC) consisting of a widely tunable laser master oscillator feeding an array of integrated semiconductor optical amplifiers that are interferometrically combined on-chip in a single-mode waveguide is shown. We demonstrate a stable and efficient on-chip coherent beam combination and obtain up to 240 mW average power from the monolithic PIC, with 30–50 kHz Schawlow-Townes linewidths and >180 mW average power across the extended C-band. We also explored hybrid integration of the InP-based laser and amplifier array PIC with a high quality factor silicon nitride microring resonator. We observe lasing based on gain from the interferometrically combined amplifier array in an external cavity formed via feedback from the silicon nitride microresonator chip; this configuration results in narrowing of the Schawlow-Townes linewidth to 3 kHz with 37.9 mW average power at the SiN output facet. The pulse shaping was achieved using an InP ultrafast optical pulse shaper fabricated by Infinera corporation. In this work we report characterization of a 48 channel InP shaper at 50 GHz channel spacing, provisioned with both channel-by-channel phase adjusters and SOA gain elements. To our knowledge this constitutes the first demonstration of an operable integrated InP pulse shaper with independent intensity and phase control.

1. INTRODUCTION[1]

Photonic integrated circuits (PICs) have been an active area of research towards dramatically improved compactness and integration of subsystems into a single package. This yielded improved performance due to faster electro-optic responses, tighter electronic packaging, and smaller optical resonators for improved nonlinearity and electronic repetition rate optical pulse generation. A few examples follow.

Optical frequency combs as frequency rulers via f-2f self-referencing to form stable references; compact microresonators produce frequency combs with spectral breadths spanning an octave, with high-repetition rates bridging to the electrical domain [3]. In addition, enhanced nonlinearities in microring resonators have been used for compact, narrow linewidth sources towards dramatic lasing improvements for clock distribution and communications applications [4], [5]. In the context of coherent communications, InP platforms have developed system-on-chip systems, with both transmitter and receivers in the same package, co-packaged with high-bandwidth drive circuitry [6], [7]. The InP platform has developed competition in the hybrid silicon photonic platform, with a suite of PIC design elements towards coherent communications system-on-chip PICs [8]. These foundry platforms have also enabled application specific photonic integrated circuit development, using telecommunications oriented technology as a foundation.

Diode lasers producing both high power, good spatial and spectral mode have been of continuing interest. Beam combining offering the possibility to push beyond single emitter powers have been studied for several applications [9], [10]. In coherent beam combining, light from an array of coherent sources oscillating at a common wavelength interferes constructively to form a single beam, usually in the far-field. For good results, this requires control of the relative optical path lengths at a sub-wavelength level; this is technically demanding for radiation in the optical domain. Wavelength combining approaches, in which different array elements provide light at different wavelengths are well known, however this is not suitable for narrow linewidth single frequency applications. Beam combining research has typically

[1]↑Portions of this chapter were modified from references [1], [2].

targeted free-space applications, such as directed energy, free-space optical communications including deep-space communications, and active optical sensing such as coherent lidar.

Developments in integrated photonics have given rise to new demands for high power, narrow linewidth sources that can be integrated with on-chip single-mode waveguide platforms. In addition to high spectral efficiency coherent fiber communications and radio-frequency photonics applications, nonlinear integrated photonic applications are of particular relevance. Such applications include wavelength conversion, parametric amplification, microresonator frequency combs, and photon pair generation, as well as chip-scale atom traps. Although such integrated photonics applications generally operate at powers substantially lower than do the free-space applications above, the powers required often exceed those available with existing on-chip sources.

Microresonator frequency comb generation, in which continuous-wave pumping of a high quality factor microresonator gives rise to formation of combs of optical frequencies spaced by tens to hundreds of gigahertz arise due to nonlinear wave mixing mediated by the optical Kerr effect and are frequently termed Kerr combs [11], [12]. Mode-locked laser frequency combs [13] have had revolutionary impact in optical frequency metrology, spectroscopy, and other applications, but are generally too bulky for large scale applications outside the laboratory [13]. Since their observation more than a dozen years ago [14], Kerr combs have been the focus of an intense research effort, in large part due to their potential as a compact and widely deployable frequency comb solution. However, Kerr combs have usually been pumped with external cavity lasers or other off-chip sources, often in conjunction with fiber amplifiers, both to achieve the necessary power and to provide the tunability and narrow linewidth necessary for efficient coupling into the resonant mode. Recently, low noise Kerr comb generation has been achieved by directly coupling a semiconductor gain element to a silicon nitride (SiN) microring resonator [15]–[17]; such work represents important progress toward truly compact and portable comb systems. Nevertheless, significantly stronger pump powers are still desirable to realize high power comb states, such as those from normal dispersion microresonators [18], [19], that can be advantageous for applications such as radio-frequency photonics [20] and high-order coherent communications [21], [22]. High power,

narrow linewidth pump sources are also advantageous for cascaded electro-optic [23], [24] or resonant [25] electro-optic comb generators.

Laser sources for integrated photonics include monolithically integrated lasers in III-V materials platforms, heterogeneously or hybrid integrated III-V lasers for silicon photonics, and rare-earth doped silicon photonic waveguide lasers [26] which require optical pumping and will not be discussed further. As an example of monolithic integration, arrays of tunable lasers, modulators, power monitors, photodetectors and other elements have been fabricated in indium phosphide to realize transmitter and receiver photonic integrated circuits (PICs) for coherent wavelength division multiplexed fiber communications [6], [7]. Alternatively, silicon photonics seeks to bring the advantages of advanced silicon manufacturing infrastructure to photonics applications, but must rely on III-V materials for on-chip light sources since silicon is an indirect bandgap material. This can be achieved either by a heterogeneous integration approach, which in which arrays of III-V chips are bonded to silicon and then processed at the wafer scale, or by a hybrid integration approach, in which different dies are first processed, then aligned and attached or bonded onto a common substrate [8], [27]. Both the monolithic and III-V silicon approaches feature lasers that can be tuned throughout the lightwave C-band at power levels of at most a few tens of mW, with high side-mode suppression ratios and relatively narrow linewidths. Reference [28] reported an InP reflective semiconductor optical amplifier (R-SOA) butt-coupled to a SiN microring resonator chip, achieving a laser linewidth of 13 kHz with 1.7 mW output power. Reference [29] reported multi-chip hybrid integration using butt-coupling between a silicon microring resonator filter chip and III-V gain chip to the laser cavity, which is then coupled to a III-V booster amplifier chip, with an impressive 100 mW fiber-coupled power and linewidth below 15 kHz across the C-band.

Substantial effort has been invested in development of monolithic InP devices capable of simultaneous high power and narrow linewidth performance. Monolithic master oscillator power amplifier (M-MOPA) architectures featuring a master laser feeding an amplifier with expanded spatial mode or an amplifier array with far-field coherent combination have yielded diffraction-limited CW output power beyond 1 W into free-space [30]. More recent works have reconsidered amplifier arrays in integrated photonics for coherent beam combination.

For example, one monolithic InP device features a DFB laser that splits to feed a four-element amplifier array [31] that outputs >100 mW into free space. Reference [32], which represents a much higher level of integration, describes a fully-integrated free-space beam steering chip using hybrid III-V silicon technology. The chip comprises a tunable laser and preamplifier, which is split and directed through an array of channel amplifiers to feed a 32-element surface grating array. The powers in the channel amplifiers are not specified but are expected to be low enough to avoid gain saturation. Coherent beam combining is achieved through far-field propagation, with beam steering implemented in one direction via channel-by-channel phase control and in the orthogonal direction via wavelength tuning and grating diffraction. In contrast to these devices which radiate into free-space, reference [33] uses a hybrid InP-SiN platform for coherent beam combining into a single waveguide mode. Two InP reflective SOAs are coherently phased by coupling to a common SiN waveguide that forms part of the laser feedback path. 4 mW of output power is reported, with 92% combining efficiency and 350 kHz linewidth. Another work uses discrete polarization beam splitter to implement a polarization-diversity amplification scheme, in which orthogonally polarized beams first counter-propagate through a single amplifier chip and then recombine into a single spatial mode [34].

In addition to high performance transmitters (i.e. lasers), integrated receivers have been developed in support of coherent wavelength division multiplexing communications. Integrated wavelength demultiplexing components, such as arrayed waveguide gratings (AWGs) [35], or resonator arrays [36] have been implemented in foundry compatible processes [37], [38]. In the context of optical frequency combs, arbitrary pulse shaping [39] has been implemented via demultiplexing, shaping individual optical frequency comb lines, then recombining. Modern pulse shaping work has grown to make use of the photonic integrated circuit platform. For example, reference [40] shows thermo-optic control, however the pulse shaper update rate was limited by the thermal update rate. In pursuit of improved update speed, reference [41] showed 1 μs update rate applied to a RF photonic filter, showing amplitude shaping with sufficient fidelity for 35 dB suppression in an RF photonic filter, as well as μs update rate.

In this work I report testing results of InP photonic integrated circuits fabricated by Infinera. I characterized an InP high-power widely tunable laser and integrated pulse shaper, the second generation device to the one shown in [41].

2. INP HIGH-POWER WIDELY TUNABLE LASER MONOLITHICALLY INTEGRATED WITH SOA ARRAY[1]

2.1 Introduction

This work was a collaboration between Professor Andrew Weiner's research group, Professor Minghao Qi's, research group, and Infinera corporation. In this work, I tested InP laser devices fabricated provided by Infinera corporation. Results on this device are reported here. Later, Professor Minghao Qi's group provided a high-quality factor SiN, which Infinera corporation then butt-coupled to the final iteration laser, to form the hybrid laser device.

2.2 Device Structures

The InP-based photonic integrated circuits (PIC) are fabricated using a system on chip PIC integration platform that monolithically integrates high gain active sections and low-loss passive waveguides. The active elements consist of multi-quantum well (MQW) active regions whereas the passive regions (waveguides and MMIs) consist of bulk double heterostructures. Conventional growth-etch-regrowth techniques [7] are used to monolithically integrate the different components of the widely tunable, narrow linewidth master oscillator with an array of SOAs. After the epitaxial (re)growths and front-end wafer fabrication (patterning and etching) are complete, the PIC wafers are subjected to a back-end wafer fabrication process sequence to define the active/passive waveguide and form inter-device and channel–channel electrical isolation, contacts and regions of the active devices. Once the wafer fabrication steps are complete, the wafers are subjected to a die fabrication sequence wherein they are singulated into individual die (via cleaving) and each die is coated with an anti-reflection coating. The die are subsequently solder die-attached to a chip-on-carrier (CoC).

The widely tunable master oscillator used was an experimental variation of a DBR-type commercial laser previously described in [7] and most recently optimized as a foundry offering [42]. The device featured differentially tuned grating mirrors with reflection combs

[1]↑Substantial portions of this chapter were published in reference [1].

of different spectral spacing enabling Vernier tuning over the extended C-band [7] and quasi-continuous tuning over 5 nm.

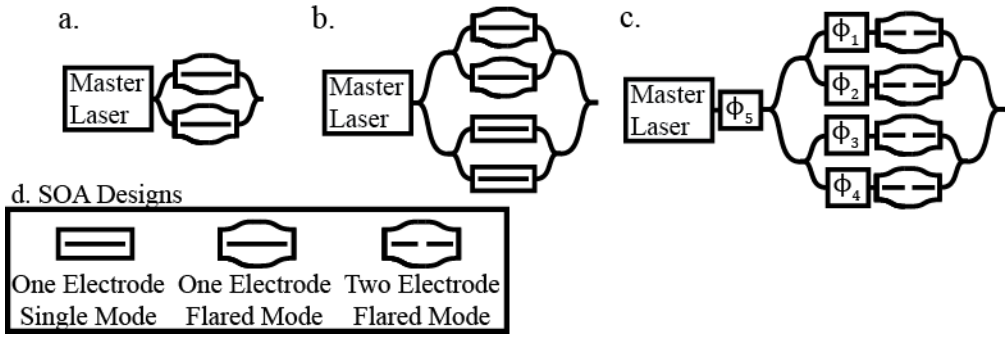

Figure 2.1. a. Dual SOA architecture utilizing single electrode SOA variant. b. quad SOA architecture with mixed SOA designs. c. quad SOA architecture with integrated phase adjusters ($\phi_1 - \phi_4$) for coherent combination and linewidth control (ϕ_5). d. summary of SOA variants tested.

The widely tunable master oscillator was integrated with an array of SOAs. In this work we demonstrate coherent combination of four SOAs on a single PIC, although there is no fundamental limit to scaling to a larger number of SOAs. InP PICs are typically realized using a high-confinement-factor integration platform to achieve maximum modal gain for lasers and high efficiency for modulators and photodetectors. Thus, the coherent combination of an SOA array approach was implemented to scale the output power beyond the saturation power of individual SOAs in this integration platform. Three successive PIC designs were explored to optimize the power from the interferometric combination of SOAs. The first PIC featured two SOAs (dual SOA), with the relative phase between each SOA controlled via the drive currents to the individual SOAs. Two dual SOA variants were fabricated and compared; one variant featured two SOAs with single electrodes of constant transverse mode size, while the second variant consisted of two SOAs with a flared optical mode to adiabatically increase then decrease the transverse mode profile in an attempt to boost the SOA saturation power [43]. The latter variant is shown in Figure 2.1a, referred herein as dual SOA with flared electrode design.

The second iteration consisted of four SOAs (quad SOA) as shown in Figure 2.1b. The architecture featured a mix of two SOA pairs: the variant with constant transverse mode and

the single electrode flared transverse mode design. The relative phase was again controlled by changing each SOA bias current, as previously shown in master oscillator power amplifier literature [44].

The third iteration integrated thermo-optic phase adjusters with an array of four segmented flared SOAs, shown in Figure 2.1c, called the two electrode flared mode design. The SOA electrode was segmented and flared to control the injected current density across the SOA, and four thermo-optic phase adjusters were used to independently control the phase to achieve coherent combination ($\phi_1, \phi_2, \phi_3, \phi_4$) [42], [45].

All the designs featured an angled output waveguide with an anti-reflective coating to suppress reflections from the InP-air interface. Despite high reflection suppression, small reflections that pass through the SOA array are amplified and fed back into the laser. Feedback amplitude as low as -90 dB has been shown to impact lasing coherence and linewidth depending on feedback phase [46], [47]. To control the phase from the InP-air interface, on the third iteration a thermo-optic phase adjuster (ϕ_5) was incorporated between the master laser and the SOA array for linewidth control. We will refer to the ϕ_5 element as an external cavity phase adjuster since it is situated outside the master oscillator laser cavity.

2.3 Optical Power Testing

We now report on the optical power performance of the master oscillator – interferometric power amplifier PICs from the three successive design cycles. For the first PIC, which utilized single electrode flared SOAs in a two-arm interferometer (Figure 2.1a), we used an integrating sphere (Thorlabs S144C) to collect and measure the output power. The PIC were tested in a chip on carrier (CoC) configuration where the laser PIC was soldered to a customized AlN carrier featuring wire-bonding between the die and carrier in addition to a soldered carrier thermistor for active temperature control. The CoC were mounted on a customized temperature controlled vacuum chuck with a temperature stability of +/- 0.01 C. A custom optoelectronic probe station was built to permit alignment of an output optical fiber, multiple individual DC probes, and a custom high density probe card. Additionally, a home-built high density driver was used to provide the required PIC control signals. The

relative phase between the interferometer arms was controlled by adjusting the SOA biases as no independent DC- phase adjusting elements were included in this design. The measured output power, plotted in Figure 2.1a for SOA currents between 0-350 mA, shows an obvious interferometric variation. For SOA currents above roughly 200 mA, peak power is achieved roughly along contours of constant current difference. Figure 2.2b shows a cut through the data of Figure 2.2a for SOA2 current fixed at 322 mA, 92% of its maximum value. In the high drive current region, we observe a maximum power of 110mW and a minimum showing over 20 dB of interferometric extinction. Local power maxima occur at SOA #1 currents of 240 mA and 325 mA, indicating 2π phase variation over this range of currents. The PIC also included a variant in which single electrode, constant transverse mode size SOAs were placed in the two-arm interferometer; this configuration resulted in a maximum output power of 99 mW. The two-arm interferometer using the single electrode design with flared mode had higher output power and is the design reported here.

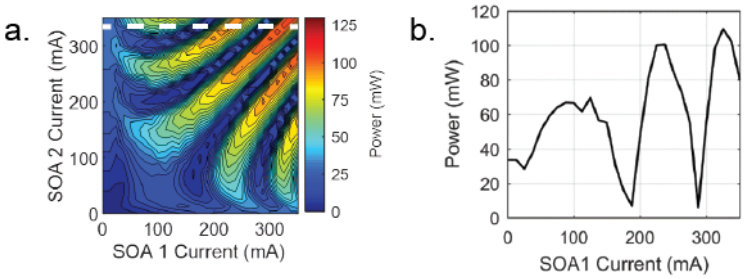

Figure 2.2. a. Interferometrically combined 2 SOA power plot, showing interference pattern for the 2 SOA devices. 2b. Cross-section of the interference, showing over 20 dB extinction.

The second-generation PIC featured four SOAs with mixed designs, as shown in Figure 2.1b. This iteration included a variation to the epitaxial layer of the dual SOA design to reduce optical mode confinement in the active region. By reducing the confinement factor, the gain coefficient is smaller, therefore reaching saturation at a higher carrier density but requiring a longer length SOA element to provide high gain. Each PIC integrated two single electrode flared optical mode SOAs and two single electrode SOAs with constant transverse mode size, thus the mixed SOAs in the quad interferometer. The power was coherently combined using nested Mach-Zehnder interferometers, with relative phases controlled using SOA

bias current. During testing, the output power was measured using the integrating sphere when up to three SOAs were driven. The physical size of the integrating sphere did not leave enough room to bring in four electrical probes. Therefore, in experiments in which we drove all four SOAs, we relied on coupling to a lensed fiber for optical power measurements. In these cases, we periodically tweaked the position of the lensed fiber to compensate for mechanical drifts of the setup. We calibrated the InP to lensed fiber coupling loss by comparing the free-space power collected with the integrating sphere (Thorlabs S144C) and with the lensed fiber power, with only a single SOA driven. The coupling loss with lensed fiber is measured to be 3 dB. This was used to compute the facet power during 4 SOA coherent combination.

In this architecture, the SOA bias provided both gain and phase shift control. Since the interferometer arms are not perfectly balanced, due to fabrication-related fluctuations in path length, some of the SOAs must be run below maximum current (hence below maximum power) to achieve phase matching for coherent combination. This introduces a trade-off between phase and output power per device. To find the optimum current settings, we implemented an iterative hill-climbing algorithm to find the maximum power, nearest to the maximum bias. The algorithm is analogous to direct binary search in digital hologram design [48]. In this analogy, the digitally designed hologram iteratively adjusts phase mask pixels and keeps changes that maximally reduce the errors in the expected reconstructed image. In our implementation, the algorithm first initializes the SOAs at maximum bias (initializing the phase mask), and then increments the SOA biases in order to find the local power maximum (minimizing phase error). After initializing, the algorithm samples the output power with a lensed fiber, increments an SOA bias, samples power, records the change, and then resets the SOA bias. This process is repeated for the next 3 SOAs, and the largest increase in output power is kept. The incrementing is repeated until no further increases are found, then the increment is halved, and the process repeated until increases in power fall below the amplitude noise. This algorithm was previously utilized in coherent combination of an integrated-optic traveling-wave-amplifier array of 10 amplifiers [49]. Experimental results are shown in Figure 2.3a for coherent combining of three as well as four SOAs. In both cases the maximum power plateaus in less than fifteen iterations of the algorithm. When three SOAs

are driven, we attain 90 mW power measured via the integrating sphere. The output power is then monitored continuously over a thirty-minute period without further changes to the SOA currents. The power remains constant, demonstrating the excellent passive stability of the integrated Mach-Zehnder interferometer (Figure 2.3b).

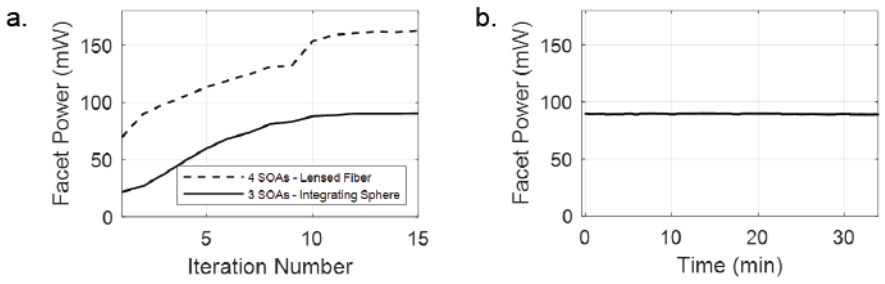

Figure 2.3. a. Plot of coherent combination of 4 SOAs measured with lensed fiber, and 3 SOAs measured in free space. b. Free-space power for 3 SOAs measured over a 30 minute interval, showing stable coherent combination over time.

The measurement was repeated with 4 SOAs, with the power sampled using lensed fiber. In order to implement coherent combination, the iterative method was stopped after 9 iterations to recouple the lensed fiber, and then continued to reach a maximum of 81mW in fiber (162 mW after accounting for the 3 dB coupling efficiency). The 16:9 ratio of output powers with 4 and 3 SOAs is consistent with the expected scaling relation discussed below. As shown in Figure 2.1b, the device features a mixed set of SOA designs with different maximum powers. When a single SOA is driven at maximum current, the single electrode flared mode design gives 55 mW per SOA, while the single electrode constant transverse mode design provides 49.5 mW per SOA. Although with perfect coherent combination, we expect 209 mW output power, we only measured 162 mW, 77% of the expected output power. We believe the power was lost due to decrease in SOA bias as much as 33% in order to optimize the coherent combination. Based on this observation, on-chip phase adjusters were integrated in the next design to minimize power lost when coherently combining the SOAs.

The third generation PICs consisted of four SOAs in the flared mode configuration. Each SOA gain region was segmented into two equal lengths with separate electrodes to

improve the spatial control of the carrier density along the length of the SOA device, which simultaneously increases saturation power and reduces noise figure [45]. In addition, the design included integrated thermo-optic phase adjusters inside the nested Mach-Zehnder interferometer to compensate for phase differences between the arms and power lost due to SOA drive variations. Figure 2.4 shows the output power for a single SOA (others left open) measured with an integrating sphere, for different currents to the front and back SOA segments. The laser's tuning elements were left open, leaving the laser at 1537 nm instead of the designed gain center of 1542 nm. We show that equal drive to both SOA segments gives the maximum output power, with an estimated single SOA power of 76 mW; this value is obtained by multiplying the measured power by a factor of four to account for the 6 dB loss that the output of a single SOA encounters in passing through two 3 dB couplers in exiting from the nested interferometers. This represents a 38% increase in SOA saturation power, compared to the 55 mW maximum per single electrode SOA measured in the 2 SOA PIC design (second generation design). We attribute this increase to control of current density across the gain region.

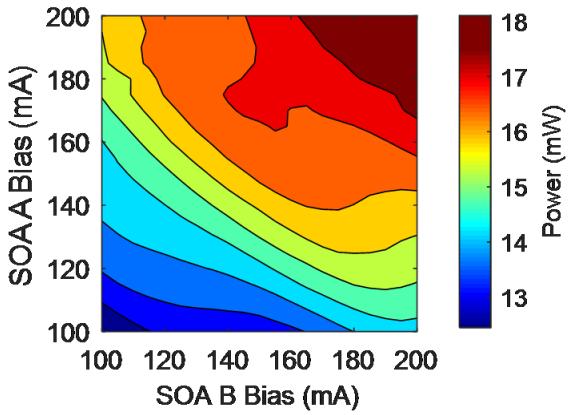

Figure 2.4. Measured facet power for the third generation PIC vs. input segment (A) bias and ouptut segment (B) bias. Only a single SOA is excited.

In order to investigate the coherent combination performance of the third generation PICs, the laser is tuned to the center of the gain spectrum (1542 nm), and measurements are performed with various numbers (N) of SOAs excited. The SOAs employed are biased symmetrically (equal current to each electrode); unused SOAs are left open circuited. The

thermo-optic phase adjusters were iteratively adjusted for maximum power output, using the algorithm described above. After reaching the maximum power, the phase of one of the thermo-optic phase adjusters was swept in order to observe the interference of one SOA against the $N-1$ SOAs that remain coherently combined. We can understand the power scaling with the number of SOAs excited (N) as follows. First, assuming each SOA generates the same output power P_0, ideal power combining yields an output power that scales linearly with N, i.e., $Pout = NP_0$. However, each of our SOAs is embedded in an M arm interferometer interferometer (NM), i.e., one SOA in each of M interferometer arms. Then with one SOA on only, we get an out of only P_0/M, where the $1/M$ is the loss that one SOA incurs in going through the interferometer output coupling regions. If we have N out of the M SOAs on and perfectly in phase, then we add N fields and square, so the output power is

$$P_{out} = \frac{N^2 P_0}{M} \tag{2.1}$$

We see that the output power scales quadratically with the number of SOAs excited inside the M-arm interferometer. When all of the SOAs are turned on, we have $N = M$ and obtain the expected $P_{out} = NP_0$. If in a similar way we have N SOAs turned on, but one is exactly out of phase with all the others ($2 <= N <= M$), the resultant output power is given by

$$\mathrm{P}_{out} = \frac{(N-2)^2 P_0}{M} \tag{2.2}$$

For our experiments $M = 4$, and the interference contrast (maximum to minimum power ratio) is expected to be 1:0, 9:1, and 4:1, for N = 2,3, and 4, respectively.

Figure 2.5 shows the resultant interference curves. In the two SOA case, we measured a 20 dB extinction ratio, with a maximum power of 72.48 mW, showing near balance in the individual SOA contributions (Figure 2.5a). For three SOAs, the maximum power with coherent combination reached 151 mW, with an extinction ratio of 9.5 dB for equal SOA output powers with 3 out of 4 SOAs powered. For four SOAs, the maximum power was 240 mW, and an extinction of 6.8 dB was measured averaged over the four interference traces which is close to the expected value of 6dB. These results provide evidence of high-

quality control of the coherent combination process with the integrated independent DC phase controls. Note that the variations in maximum powers and extinction over the full range of phase shifts is attributed to mechanical drifting of the lensed fiber relative to the chip during the measurement.

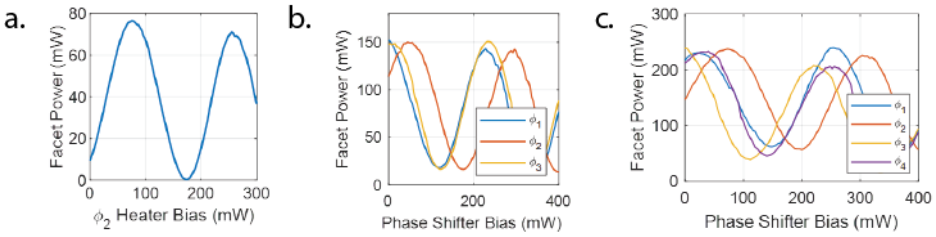

Figure 2.5. The representative curves with a. 2 SOA, b. 3 SOA, c. 4 SOA coherent combination on chip, showing the measured converged power levels.

Table 2.1 compares the maximum powers obtained vs. number of SOAs excited (N) to the values predicted for ideal coherent combination from equation 2.2. The single SOA power (P_0) was measured with one SOA excited using symmetric current biases of 200 mA per electrode, and the other SOAs open left open. This measurement was performed for each of the four SOAs. The average value and standard deviation between 4 SOAs, 18.98 mW $\pm$ 0.89 mW, is reported in Table 1. This number was extrapolated to 2, 3, and 4 SOAs using the equation above to yield the expected power. Roughly we do see the expected N^2 power scaling. However, we note that the actual power for $N = 4$ is about 21% below the estimated ideal value, which we believe can be attributed to thermal effects.

Table 2.1. Measured power scaling for the fully combined PIC as a function of the number of SOAs excited (N)

Wavelength: 1542 nm	Facet Power (mW)		
N SOAs	Measured	Expected	$\frac{P_{Meas}}{P_{Expected}}$(%)
1	18.98 $\pm$0.89	–	–
2	72.48	76	95
3	150.56	171	88
4	240.04	304	79

2.4 Widely Tunable Narrow Linewidth Pump Laser

We now present data on the tunability, spectral purity, and linewidth of the tunable laser, both with and without high power amplification. The master laser is a custom variation of a commercially available widely tunable sampled grating tunable distributed feedback laser [7]. The laser is coarsely tunable by differential thermal control of the mirror gratings; fine tuning is achieved with an intracavity thermo-optic phase adjuster. Figure 2.6a shows the coarse tuning characteristics of the laser over the extended C-band from 1503 nm through 1568 nm. Here in order to avoid any effects that might be associated with high power SOA operation, a single SOA is current biased just below transparency to provide a measurable output while the other three SOAs are short-circuited for a high absorption state. Fine tuning over a range of 0.25 nm using the intracavity phase shifter is shown in Figure 2.6b, with wavelength measured using a commercial wavemeter (HighFinesse WS6-100).

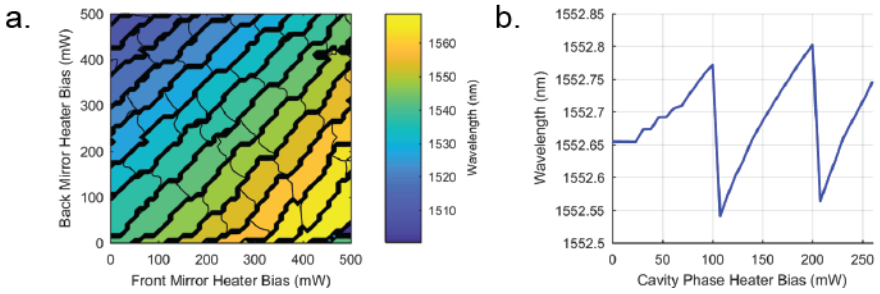

Figure 2.6. a. Coarse tuning wavelength map of the laser output. b. Fine tuning measured wavelength output.

Figure 2.7 shows data on output power and side mode suppression as the laser is coarsely tuned, both with and without amplification. Figures 2.7a and 2.7b provide two different views of the spectral performance without amplification, measured using an OSA set for 1.2 GHz spectral resolution. The laser maintains over 60 dB side mode suppression ratio over the extended C band. Note that the low output powers shown are the result of absorption in the SOA array. Figures 2.7c and 2.7d show similar data for the laser output after iterative power combination of the fully biased SOAs. At the center of the gain spectrum (1542 nm), the facet power was 240 mW, and the side mode suppression ratio remained at 60dB even under this full amplification condition. When the laser was tuned to the spectral edges of

1513 nm and 1568 nm, the facet powers dropped to 180 mW with a side mode suppression ratio of 42 dB.

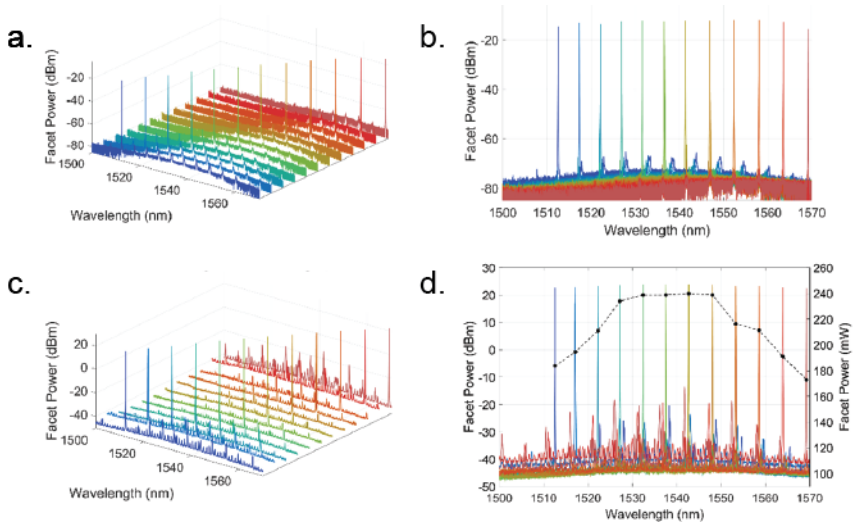

Figure 2.7. a. and b. Measured OSA tuning spectra at low power (only a single SOA is on, biased below transparency). c. and d. Optical spectra measured with SOAs biased at full current and phased for maximum output power with phase adjuster ϕ_5 tuned for minimum linewidth. In d. the facet power is given in both logarithmic and linear scales.

Next we discuss measurements of the laser linewidth and frequency noise. The master laser's high frequency equivalent linewidth is expected to be of order 200 kHz, similar that of its commercial variant. However, it is well known that feedback at levels as low as -90 dB, e.g., due to reflection from the InP-air interface, can produce linewidth broadening, multimode lasing, or linewidth narrowing depending on the phase of the reflected signal [46], [47]. These effects may be more pronounced if there is gain in the feedback path, as is the case here. Using the tunable phase adjuster labeled ϕ_5 in Figure 2.1c, we can maintain and indeed reduce the laser linewidth even under full amplification conditions, as demonstrated in the following.

Laser linewidths are typically obtained via a delayed self-heterodyne signal which is measured on an RF spectral analyzer [50], [51]. However, this technique measures a lineshape function that convolves technical noise terms with the intrinsic Lorentzian line shape, also called the Schawlow-Townes linewidth, fundamental linewidth, or high frequency equivalent

linewidth in literature [4], [52]–[55]. Technical noise originates from outside the laser cavity and includes factors such as electrical driving noise and environmental noise coupling into the delayed self-heterodyne instrument [56]. These factors can be reduced with sufficient engineering and stabilization techniques for improved long term laser stability and instrument performance at the expense of setup complexity [57], [58]. When trying to retrieve the fundamental linewidth from a delayed self-heterodyne dataset, the technical noise is accounted for one of two ways: either by estimation from the 20 dB linewidth or by fitting a Voigt lineshape to the dataset which approximates the technical noise as Gaussian [55], [59]. When both the Schawlow-Townes linewidth and technical noise contribution have the same 3 dB linewidth, the Gaussian approximation for technical noise breaks down; and the technical noise obscures the Schawlow-Townes lineshape contribution [55]. With improved photon lifetime, the lineshape will converge to a residual lineshape originating from technical noise [52].

The technical noise's contribution can be handled instead by measuring the laser's frequency noise power spectral density. One method uses a frequency discriminator at quadrature bias to map the laser's frequency fluctuations to intensity with spectral content showing the laser's frequency noise power spectral density. Measured this way, the flicker noise contribution goes as 1/f with frequency, and the Schawlow-Townes linewidth contribution manifests as a broadband (white) noise level extending to the relaxation oscillation frequency [60]. This represents a direct measurement of the Schawlow-Townes linewidth and technical noise independently, improving precision and enabling linewidth computation for different time scales [52], [61]–[63]. Here we implemented a modified delayed self-heterodyne instrument that measures the frequency noise power spectral density for precise measurement of the Schawlow-Townes linewidth as follows.

Our measurement apparatus, sketched in Figure 2.8, follows an approach developed in [64]. The input signal (laser under test with angular frequency ω_0 and phase noise $\phi_n(t)$) is split into two arms; the first arm features a fiber delay line (20 km of smf-28e, corresponding to 100 μs delay). The second arm features and electro-optic phase modulator, driven to produce the phase modulation, $\phi_{mod}(t) = bsin(\omega_c t + \phi_c)$, where b is the modulation index in radians and ω_c and ϕ_c are the angular frequency and phase of the RF drive. We set the

RF frequency to 500 MHz, limited by the oscilloscope bandwidth and set modulation depth b to 2.63 for balanced I/Q outputs. The signal at the output of the interferometer (power P) was incident on a photodiode (responsivity Re) and recorded on a real-time oscilloscope (Rhode & Schwarz 1024, 2 GHz analog bandwidth at 10 GS/s). The photodetected signal contains harmonics at angular frequencies ω_c $2\omega_c$, convolved with the laser's lineshape with 3 dB linewidth of $\delta\nu_{3dB}$. These harmonics together enable retrieval of the laser's differential phase noise, $\Delta\phi(t)$, where $\Delta\phi(t) = \phi_n(t) - \phi_n(t - \tau_d)$ for $1 \ll \tau_d\Delta\nu_{3dB}$, so that $\phi_n(t)$ and $\phi_n(t - \tau_d)$ are uncorrelated [63]. In particular, the harmonics at ω_c and $2\omega_c$ may be written as:

$$\begin{aligned} I(t) &= -J_2(b)Psin(\Delta\phi(t) + \omega_0\tau_d)cos(2(\omega_c t + \phi_c)) \\ Q(t) &= J_1(b)Pcos(\Delta\phi(t) + \omega_0\tau_d)sin(\omega_c t + \phi_c) \end{aligned} \tag{2.3}$$

The $I(t)$ and $Q(t)$ signals, at frequencies $2\omega_c$ and ω_c, respectively, were processed offline using the software coherent receiver structure shown in the dashed line in Figure 2.8. Both signals are demodulated down to baseband and filtered with a linear-phase finite impulse response (FIR) lowpass filter with cutoff below $\omega_c/2$ to prevent cross-talk between the signals $I(t)$ and $Q(t)$; this sets the measurement bandwidth and can be increased by drive the phase modulator at a higher frequency. $I(t)$ and $Q(t)$ are recombined to give the laser's differential phase noise, $\Delta\phi(t)$. For further details, please refer to reference [63]. Taking the time derivative of the differential phase noise yields the measured instantaneous frequency fluctuations in time. Plotting the frequency noise power spectral density allows one to directly observe the quantum (white) FM noise floor. The latter in turn can be used to compute the Schawlow-Townes linewidth [52], [63].

2.4.1 Linewidth Measurement Sensitivity

In this section we evaluate our system's measurement limits. We compare the reported device's FM noise with commercial lasers, showing capacity to resolve Schawlow-Townes linewidths below 2 kHz. Figure 2.9a shows two measured FM noise spectra - one from a commercial discrete mode laser at highest output power (Eblana Photonics EP1550-0-DM-H16-FM), the other from our device's master laser at maximum output power. Each

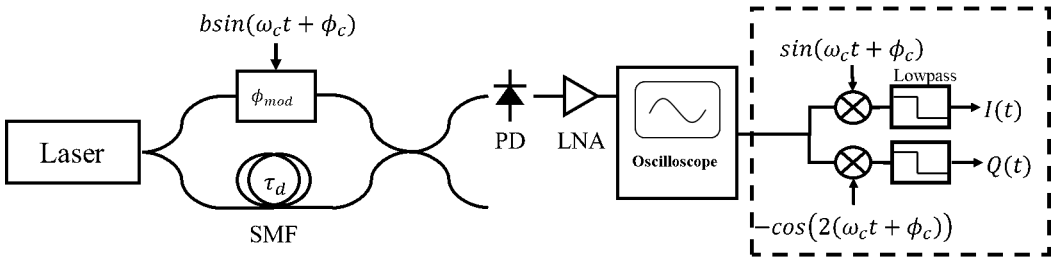

Figure 2.8. Delayed self-heterodyne setup. After passing through a delay-imbalanced interferometer with an embedded phase modulator, the signal is incident on a photodiode (PD) connected through a low noise amplifier (LNA) to a digital oscilloscope. The signal recorded on the oscilloscope is process offline for coherent reception of the differential phase noise (as sketched within the dashed lines).

offset frequency represents different noise terms. The technical noise dominates in the low frequency regime, rolling off as 1/f and is attributed to electrical noise in the laser diode gain region [60]. We compute the Schawlow-Townes linewidth $\Delta\nu_{Sch} = \pi S_0$ [63]. The instrument limits the measurement bandwidth, giving a roll off at 250 MHz, though the white FM noise is expected to continue to the relaxation oscillation frequency [60]. The quantum noise level S_0 should be inversely proportional to the laser's output power [52]. In order to show that we can retrieve the laser linewidth without saturation due to the residual linewidth from technical noise, we plot the Schawlow-Townes linewidth against output power (Figure 2.9b) [52]. The commercial discrete mode laser's Schawlow-Townes linewidth shows the expected inverse relationship $\Delta\nu \propto 1/P_{out}$ and converges to the manufacturer's specified 800 kHz Schawlow-Townes linewidth, validating our instrument's measurement. To perform the measurement on our master laser, without amplification effects, three of the SOAs were left open circuited. One electrode of the fourth SOA was forward biased just below transparency; and an on-chip detector was biased in order to measure the master laser output power. This low power sample of the master oscillator was coupled off chip into the modified delayed self-heterodyne setup, and the Schawlow-Townes linewidth was extracted. This procedure was then repeated with increased master laser cavity gain bias. In this way both laser output power and Schawlow-Townes linewidths were measured. The plot of linewidth vs. laser output power

in Figure 2.9b again exhibits the theoretically predicted linewidth of $\Delta\nu_{Sch} \propto 1/P_{out}$. This measurement demonstrates Schawlow-Townes linewidth resolution down to 100 kHz.

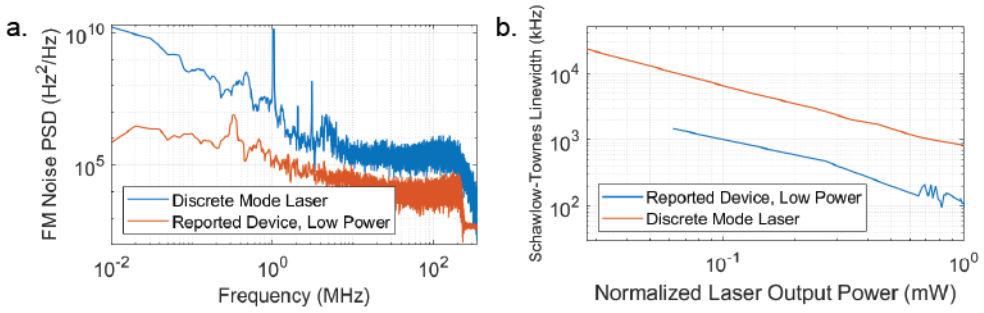

Figure 2.9. a. Comparison of the FM noise power spectral density, with the laser at low power. b. The Schawlow-Townes linewidth vs. laser output power

To characterize the sensitivity limits of our setup, in Figure 2.10 we compare the reported device's FM noise spectrum (corresponds to 1523 nm wavelength from Figure 2.9 with those that we measured from the two commercial low noise lasers. One measurement is for an external cavity diode laser (New Focus Velocity TLB-6728-P) with a rated linewidth below 200 kHz for 50 ms integration time; this value is obtained from a two laser beating experiment and is dominated by technical noise. External cavity diode lasers typically feature Schawlow-Townes linewidths below 50 kHz [65]. The high frequency plateau in our frequency noise measurement corresponds to a Schawlow-Townes linewidth at roughly the 2 kHz level. The second measurement uses a fiber laser (Orbits Lightwave INST-2500A-1542.07-5-PZ10B-T) with a specified Lorentzian (i.e., Schawlow-Townes) linewidth below 10 Hz. Our data shows a frequency noise power spectral density that drops below the 10 Hz^2/Hz level at a frequency of a few MHz, but then increases at higher frequencies with a slope of two. The slope-two increase in the FM noise floor is consistent with the oscilloscope noise floor, limited by its memory depth and ADC effective bit depth of 7 [66], [67]. The oscilloscope's white noise floor, in combination with the laser's technical noise defines the minimum resolvable Schawlow-Townes linewidth.

These results confirm that our setup has sensitivity sufficient to resolve Schawlow-Townes linewidths at the tens of kHz level reported above for our monolithic laser and amplifier array PIC; these results are also relevant for characterization of even lower FM noise operation

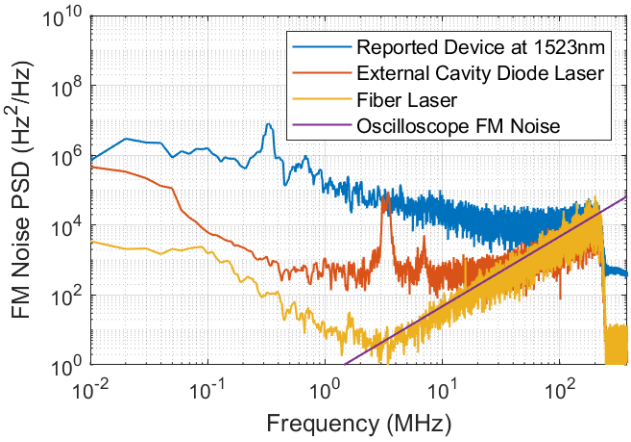

Figure 2.10. FM noise power spectral density of the reported device, compared to commercial lasers.

obtained after hybrid integration of the laser and laser amplifier PIC with a silicon nitride microring resonator, reported in the hybrid integration section.

2.4.2 Reported M-MOPA Device Linewidth Across the Extended C-band

Next we discuss measurements of the laser linewidth and frequency noise. The master laser's high frequency equivalent linewidth is expected to be of order 200 kHz, similar that of its commercial variant. However, it is well known that feedback at levels as low as -90 dB, e.g., due to reflection from the InP-air interface, can produce linewidth broadening, multimode lasing, or linewidth narrowing depending on the phase of the reflected signal [46], [47]. These effects may be more pronounced if there is gain in the feedback path, as is the case here. Using the tunable phase adjuster labeled ϕ_5 in Figure 2.1c, we can maintain and indeed reduce the laser's Schawlow-Townes linewidth even under full amplification conditions. We then measured FM noise spectra at a series of discrete wavelengths across the extended C-band, with the SOA array turned on and phased for maximum output power. As before, phase adjuster ϕ_5 was tuned to minimize the frequency noise. The extracted Schawlow-Townes linewidths are plotted in Figure 2.11.

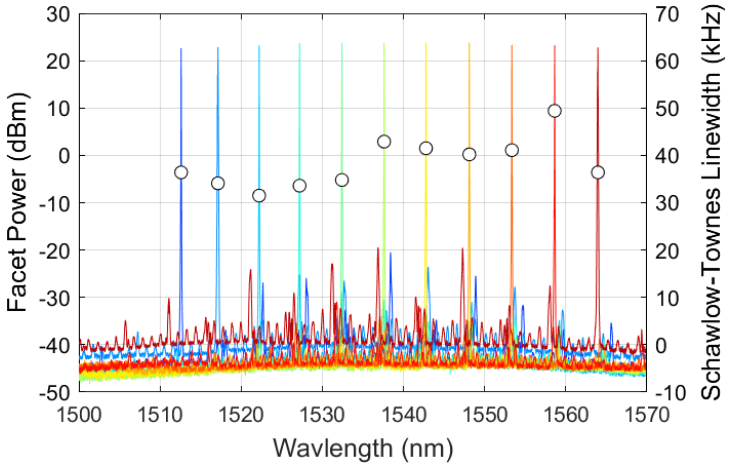

Figure 2.11. The reported device's lasing spectra, and measured linewidths.

2.5 Hybrid Integration of InP High Power Laser and SiN Microresonator

Integration of InP laser structures with microresonators in other material systems is of interest for a variety of applications. The most common motivation is to realize silicon photonic microsystems with on-chip light sources. For this purpose a popular approach is to couple an InP gain section to a silicon waveguide section containing one or more tunable ring resonator transmission filters followed by a loop mirror [8], [29]. This approach has also been pursued using silicon nitride (SiN) instead of silicon; SiN offers lower loss, resulting in higher quality factor resonators or improved grating lengths, yielding narrower laser linewidths [64], [68]. Alternatively, it is possible to use Rayleigh backscattering from ultrahigh-Q whispering gallery mode resonators has been used extensively to realize ultra-narrow linewidth from semiconductor diode lasers [69]–[71]. Rayleigh backscattering from SiN microring resonators has also been used as the end reflector for an InP semiconductor optical amplifier, resulting in laser oscillation with 2 mW facet power and 13 kHz 3 dB linewidth [28]. Kerr comb generation with stable cavity solitons was achieved via an extension of this scheme [15]. Here we report hybrid integration of the tunable InP laser and SOA array with a SiN microring resonator chip. Under high power operation feedback from the SiN microresonator chip results in an external cavity that reduces laser frequency noise, resulting in 37.9 mW facet power and Schawlow-Townes linewidth at or below 3 kHz. We attribute the increased power compared

to [28] to the interferometric SOA array which serves as the gain element in this mode of operation.

Figure 2.12 shows a schematic of the InP M-MOPA butt-coupled to a SiN microring resonator (MRR) chip. To minimize reflections back into the active components, a tilt is used for the InP waveguides relative to the facet. Due to the different refractive indices, the SiN waveguides are angled at 15° relative to the facet. For alignment purposes the InP PIC is provisioned with a DFB laser with an integrated photodetector that functions as a power monitor; the DFB laser launches light into a loop waveguide fabricated in the SiN chip that couples back to a second photodetector on the InP chip. Active alignment is performed to optimize the power recorded by the second InP photodetector. A subassembly process was developed at Infinera using an alignment system with six degrees of freedom and sub-micron positioning accuracy. The laser wafers were cleaved, and the diced pieces were AR coated. A chip on carrier (CoC) was completed by soldering the laser PIC to a customized AlN carrier and wire-bonding between the die and carrier. The SiN MRR structures used for assembly were fabricated with a "footer" to enable handling and positioning using an automated gripper tool. The SiN MRR facets used for coupling to InP were polished. Once the CoCs were completed, the lasers were paired with MRR chips. The SiN PIC was held by the gripper tool and brought into close proximity to the CoC, as shown in Figure 2.13. Algorithms were implemented to position the MRR sample through six degrees of freedom to maximize the photocurrent generated in the alignment photodetector. Once alignment was completed to an InP laser, epoxy was then wicked into the gap using capillary forces and cured using UV light.

Figure 2.12 shows several images of the MRR chips. The fabrication process is similar to that described in [72]. Briefly, resonators were formed by growing 500-800 nm thick SiN films on top of a silicon dioxide buffer layer on a silicon substrate and patterning via e-beam lithography and dry etching, after which the SiN is clad by deposition of a low temperature oxide and annealed. Unlike our previous work, however, here the silicon substrate is 0.3 mm thick, which approximately matches the thickness of the laser substrates. After fabrication the MRR chips were diced to 2 mm $\times$ 2 mm dimension suitable for assembly with the high power lasers. Figure 2.14a is a microscope image of a chip containing a MRR with 50

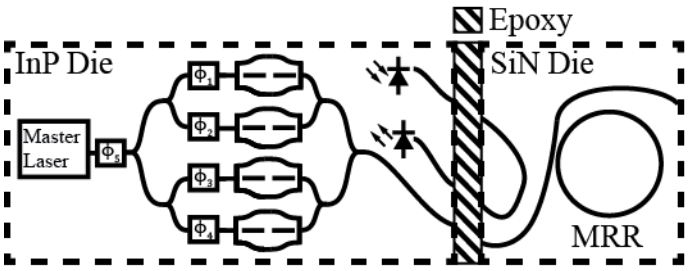

Figure 2.12. Heterogeneous integration architecture, in which various higher power laser PICs were butt-coupled to various SiN microring resonator designs. The angles of the waveguides at the facets are exaggerated.

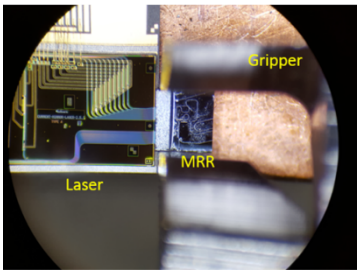

Figure 2.13. Microscope picture of laser CoC assembly, microring resonator (MRR), and gripper fixture used during alignment process.

GHz free spectral range. The "backwards J" shape of the resonator is chosen to fit within the 1 mm × 1 mm writing field of the e-beam lithography tool. In addition to the bus waveguide, which brings in laser light from the left, this MRR is also coupled to a drop port waveguide. Angling of the waveguides with respect to the facet normal and loop waveguides is also evident. A second loop waveguide (visible on the right side of the chip) was included for potential use in coupling to a second InP PIC such as an integrated pulse shaper [41]; however, we have not pursued this option. Subsequent to dicing, a 2 mm × 0.5 mm × 0.5 mm "footer" was cut from a silicon wafer and attached to the MRR chip via epoxy, Figure 2.14b. The purpose of the footer is to facilitate handling of the chips by the gripper tool. After attachment the MRR chip and footer were polished to obtain an optically smooth surface, Figure 2.14c. A micrograph showing the joint between the completed laser - MRR assembly is shown in Figure 2.14d. (In this case a different MRR chip with a circularly shaped, 99.9 GHz free spectral range microresonator was employed.)

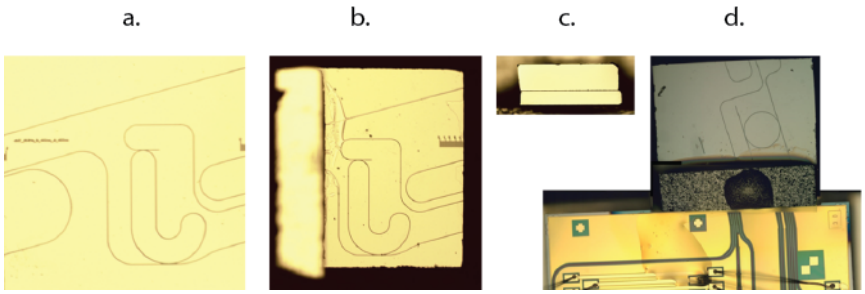

Figure 2.14. a. Representative 2mm x 2 mm microring resonator (MRR) chip. b. MRR chip after footer attachment. c. view of the MRR-footer facet after polishing. d. Completed laser - microring resonator assembly.

Four bonded InP M-MOPA – SiN MRR pairs were assembled and tested. The first three were obtained during an early assembly campaign, at which time SOA characterization was still in progress. These arrays used an SOA variant which produced suboptimum output power (160 mW). The final assembly utilized the optimized M-MOPA design capable of 240 mW output power, as reported in Section 2.3. We used two different methods to assess the InP-SiN coupling loss. One estimate was accomplished by passing the light from the integrated alignment laser through the SiN loop waveguide and back to the corresponding InP photodetector. The photodetector responsivities were pre-calibrated, and the total laser to photodetector loss was divided by two to yield the loss per facet. An independent estimate was obtained by passing the light from the tunable laser through a single SOA (the other SOAs were turned off to avoid the need to phase up the interferometers) and then all the way through the SiN chip. The output from the SiN was collected with a lensed fiber and relayed to a power meter. By pre-calibrating the laser - single SOA power and subtracting out the 3 dB SiN to lensed fiber coupling loss, we were again able to estimate the InP-SiN coupling loss. We obtained an average coupling loss of 5.1 dB, with relatively small variation (best 4.5 dB, worst 6 dB). Furthermore, the two measurement approaches provided similar results, with an average difference of only 0.4 dB. To gain further confidence, in one case we also tried injecting light from an external laser through the lensed fiber into the SiN waveguide, which in turn coupled light into the InP chip where it could be detected by using one of the SOAs reverse biased to act as a photodetector. The loss estimate was similar to that from the other methods.

Several tests were performed after the early assembly campaign to demonstrate functionality. For example, lasers were tuned quasi-continuously in order acquire transmission spectra of the attached MRR chip, using tuning data collected before hybrid integration. Figure 2.15a shows a transmission scan over a 1 nm range, obtained with a single SOA turned on at low bias. The 50 GHz free spectral range of the microresonator is clearly observed; a higher order transverse mode is also evident from the data. Note that the slope in the background (off-resonance) power is due to drift in the fiber used to collect the light coupled out of the SiN chip. Figure 2.15b shows a zoom-in of a single resonance. The 3 dB linewidth is 240 MHz, similar to that measured for the same MRR chip prior to heterogeneous integration. Reflections at the InP-SiN interface also play a role, especially when operating the SOAs for high power. Figure 2.15c shows optical spectrum analyzer data in which the laser spectrum is broadened dramatically by such optical feedback, then restored using the external cavity phase shifter ϕ_5 to the instrumental resolution (1.3 GHz) by applying a phase shift in increments of $\pi/20$. For higher resolution, we heterodyned the M-MOPA-MRR output with an external cavity reference laser, which yielded a beat note with 2 MHz linewidth at 10 dB, limited by technical noise of the reference laser. These measurements confirm the functionality of the laser PICs after microring attachment.

The final assembly using the optimized laser PIC was initially tested at low power. The output spectra and optical frequency noise were measured as the laser was tuned discretely from 1513 to 1558 nm in 5 nm increments, with only a single SOA excited weakly. At each tuning step the external cavity phase adjuster was varied to minimize the frequency noise. We observed >50 dB side-mode suppression and high frequency equivalent linewidths in the range 30 to 230 kHz, only slightly degraded compared to the performance without a bonded SiN PIC. However, the behavior was quite different at high power. With all four SOAs driven at maximum current and their respective phase shifters set for optimum coherent combination according to the iterative algorithm described previously, we were unable to achieve controllable stable single mode lasing. On the other hand, we found that if we turned off the current to the laser gain section, we could obtain high quality laser spectra. Lasing occurred near the peak of the SOA gain spectrum. Our interpretation is that under these conditions the SOA array provided the gain for a laser cavity formed by

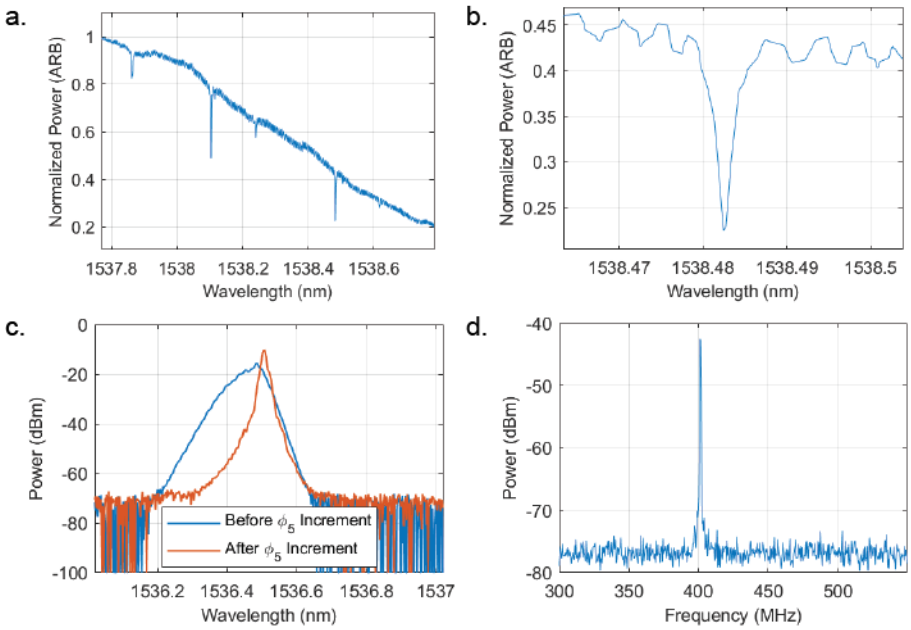

Figure 2.15. Functionality tests of early heterogeneously integrated lasers. a,b. Transmission spectra of microring resonator measured by tuning the attached laser: a. 1 nm tuning range, b. zoom-in of a single resonance. c. Optical spectrum analyzer data showing compensation of linewidth broadening using the external cavity phase shifter. d. Heterodyne beat measurement showing compensation of linewidth broadening.

the tunable laser front mirror (the one closest to the SOAs) and an external cavity resulting either a reflection from the InP-SiN interface or Rayleigh backscattering from the microring resonator. We observed that the lasing spectrum could be shifted slightly by varying the bias on the laser front mirror and cycled between 1542 nm and 1547 nm. This spacing matches the 5 nm mode spacing of the SG-DBR grating. Figure 2.16a shows optical spectra observed for two different currents to the laser front mirror. The side-mode suppression ratio approaches 56 dB, and the optical power is as high as 37.9 mW (estimated facet power just inside the SiN-air interface). We also measured the frequency noise spectrum under this lasing condition at 1542 nm, Figure 2.16b. The FM noise floor is estimated at 1000 Hz^2/Hz, which corresponds to a Schawlow-Townes linewidth of roughly 3 kHz. As the observed FM noise floor is close to the instrumental limit set by the intersection of low-frequency technical noise and oscilloscope FM noise, the actual Schawlow-Townes linewidth may be somewhat lower. Similar FM noise data are observed for 1547 nm lasing. The very

low linewidths observed strongly suggest the role of the microring resonator in reducing the frequency noise. Although this was not our original intent, these observations suggest the viability of an interferometrically combined SOA array coupled with a spectrally selective external cavity incorporating a microring resonator as a potential source for applications requiring ultralow frequency noise and significant power.

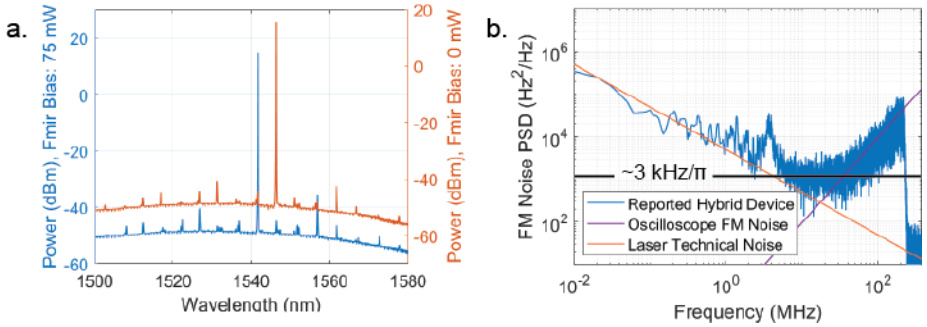

Figure 2.16. High power operation of the final laser – MRR assembly. The laser gain section was powered off; the interferometric SOA array provided the gain for laser operation. a. Optical power spectra at two different front mirror tuning currents. b. Frequency noise spectrum, from which we estimate a maximum 3 kHz Schawlow-Townes linewidth.

3. INP INTEGRATED PULSE SHAPER WITH 48 CHANNEL, 50 GHZ SPACING AMPLITUDE AND PHASE CONTROL[1]

3.1 Introduction

This device was a collaboration with Infinera corporation, who designed and fabricated the InP pulse shapers. An early device iteration with only amplitude shapers was shown in reference [41]. In this work we report characterization of a 48 channel InP loopback arrayed waveguide grating pulse shaper (AWGPS) at 50 GHz channel spacing, and some phase shaping results.

3.2 Phase Shaping

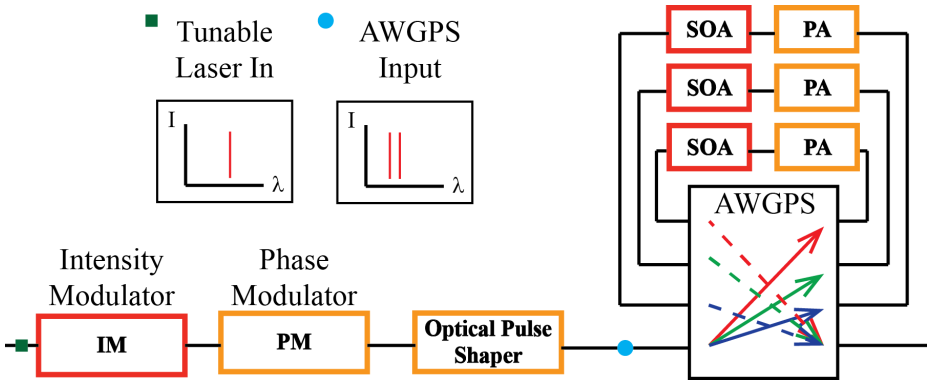

Figure 3.1. Loopback Arrayed Waveguide Grating Pulse Shaper (AWGPS) with integrated semiconductor optical amplifiers (SOA) and phase adjusters (PA). The shaped optical output was photodetected for RF time domain measurements.

To test the AWGPS phase shifting characteristics, we used an electro-optic comb source (IM and PM in Figure 3.1) with 12.5 GHz repetition rate [74], and used a conventional pulse shaper to filter out lines to yield a 50 GHz comb matched to our AWGPS. In a first experiment, the AWGPS was programmed to select just 2 lines in adjacent AWGPS channels (1 and 2) without changing the relative intensities. The two output lines were shaped in phase, photodetected to yield a 50 GHz RF tone, and measured on a sampling

[1]↑Substantial portions of this chapter were published in reference [73]

scope. Channel 1's phase bias was incremented over the full dynamic range, leading to shifts in the time domain trace, as shown in Figure 3.2a. The optical phase shift was extracted by taking the digital cross-correlation with the zero-phase shifter bias RF trace. This two-line measurement was repeated for different phase-shifter channel pairs, demonstrating nearly uniform phase shift across AWGPS channels, as shown in Figure 3.2b.

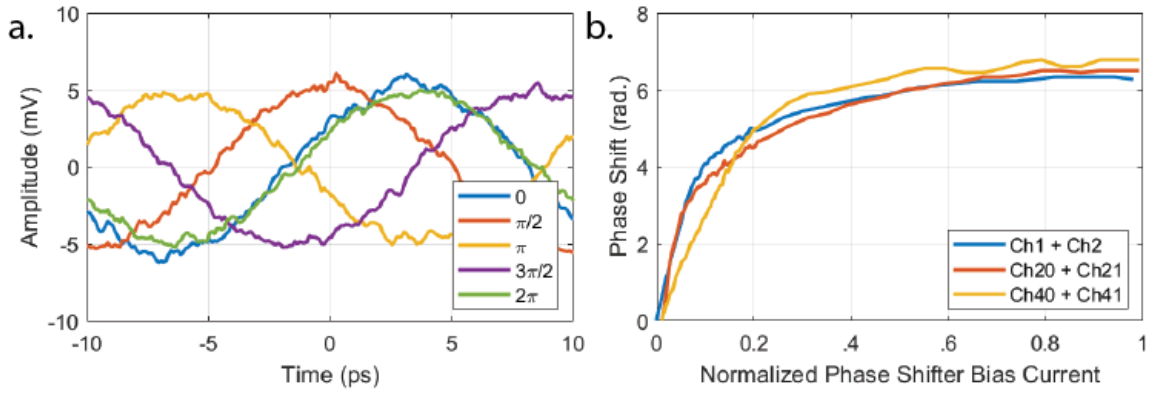

Figure 3.2. a. Measured time domain signals for phase shifter biases. b. Measured phase shift for channel pairs across AWGPS chip.

For experiments with a larger number of lines (up to 12), we used a dual comb electric field cross-correlation measurement technique, similar in spirit to [75].

The AWGPS output was interfered with a reference optical frequency comb at a different repetition rate (ERGO) such that the repetition rate difference is (Δf_{rep}); in this case Δf_{rep} is 230 MHz. The two optical signals are photodetected, resulting in a time domain waveform shown in Figure 3.3a. The power spectral density is an RF frequency comb shown produced from the vernier-like walk off of two RF frequency combs, as seen in Figure 3.3b. Each RF mode's spectral amplitude is proportional to the product of the individual AWGPS output and reference optical comb lines; the RF spectral phase is the average difference in optical phases between the signal and reference tones over the Fourier transform window. Thus knowing the reference complex amplitude and phase of the reference comb, using a method such as [76], allows one to reconstruct the signal complex envelope.

Using this method, the RF pulses were measured and plotted. To demonstrate arbitrary phase shaping, we did not characterize the reference, and assumed the reference phases were zero. To design a waveform, I first reconstructed the complex envelope in the electrical

domain, and set the phases for an odd pulse (anti-symmetric field about the carrier); both waveforms are plotted in Figure 3.4a. In these plots, the horizontal axis is linearly proportional to the optical time scale. Next the measured waveform was cross-correlated with the desired waveform to compute the inner product. This scalar was then maximized by a direct binary search algorithm, dithering the phase adjusters [48], yielding the odd pulse in Figure 3.4, showing arbitrary phase shaping.

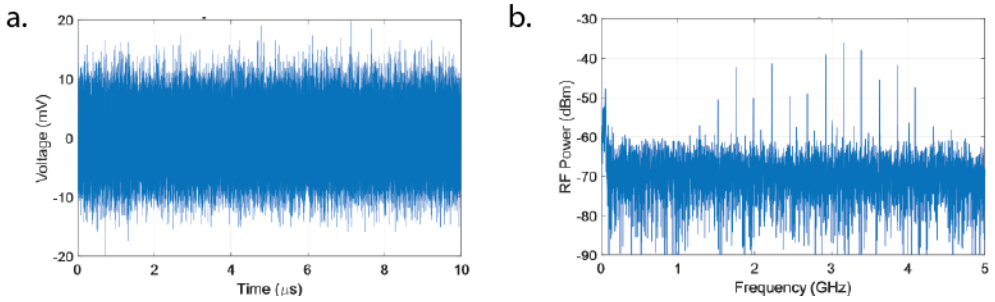

Figure 3.3. a. Measured E-field cross-correlation time domain. b. The retrieved RF spectrum. c. Pulse with no phase shifter bias. d. Pulse after some phasing bias optimization.

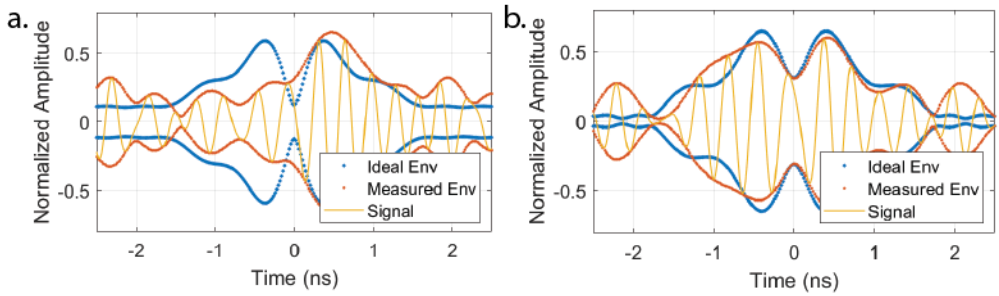

Figure 3.4. a. Pulse with no phase shifter bias. b. Pulse after some phasing bias optimization.

REFERENCES

[1] K. A. McKinzie, C. Wang, A. Al Noman, D. L. Mathine, K. Han, D. E. Leaird, G. E. Hoefler, V. Lal, F. Kish, M. Qi, and A. M. Weiner, "InP High Power Monolithically Integrated Widely Tunable Laser and SOA Array for Hybrid Integration," *Optics Express*, 2021.

[2] K. A. McKinzie, D. E. Leaird, D. Mathine, M. Anagnosti, G. E. Hoefler, Z. Kong, C. Bao, V. Lal, A. Hosseini, F. Kish, and A. M. Weiner, "InP integrated pulse shaper with 48 channel, 50 GHz spacing amplitude and phase control," in *30th Annual Conference of the IEEE Photonics Society, IPC 2017*, vol. 2017-Janua, 2017, pp. 197–198, ISBN: 9781509065783. DOI: 10.1109/IPCon.2017.8116067.

[3] D. T. Spencer, T. Drake, T. C. Briles, J. Stone, L. C. Sinclair, C. Fredrick, Q. Li, D. Westly, B. R. Ilic, A. Bluestone, N. Volet, T. Komljenovic, L. Chang, S. H. Lee, D. Y. Oh, M. G. Suh, K. Y. Yang, M. H. Pfeiffer, T. J. Kippenberg, E. Norberg, L. Theogarajan, K. Vahala, N. R. Newbury, K. Srinivasan, J. E. Bowers, S. A. Diddams, and S. B. Papp, "An optical-frequency synthesizer using integrated photonics," *Nature*, 2018, ISSN: 14764687. DOI: 10.1038/s41586-018-0065-7.

[4] S. Gundavarapu, G. M. Brodnik, M. Puckett, T. Huffman, D. Bose, R. Behunin, J. Wu, T. Qiu, C. Pinho, N. Chauhan, J. Nohava, P. T. Rakich, K. D. Nelson, M. Salit, and D. J. Blumenthal, "Sub-hertz fundamental linewidth photonic integrated Brillouin laser," *Nature Photonics*, vol. 13, no. 1, pp. 60–67, Jan. 2019, ISSN: 17494893. DOI: 10.1038/s41566-018-0313-2.

[5] G. M. Brodnik, M. W. Harrington, J. H. Dallyn, D. Bose, W. Zhang, L. Stern, P. A. Morton, R. O. Behunin, S. B. Papp, and D. J. Blumenthal, "Optically synchronized fiber links with spectrally pure integrated lasers," Feb. 2021. [Online]. Available: http://arxiv.org/abs/2102.05849.

[6] F. Kish, V. Lal, P. Evans, S. W. Corzine, M. Ziari, T. Butrie, M. Reffle, H.-S. Tsai, A. Dentai, J. Pleumeekers, M. Missey, M. Fisher, S. Murthy, R. Salvatore, P. Samra, S. Demars, N. Kim, A. James, A. Hosseini, P. Studenkov, M. Lauermann, R. Going, M. Lu, J. Zhang, J. Tang, J. Bostak, T. Vallaitis, M. Kuntz, D. Pavinski, A. Karanicolas, B. Behnia, D. Engel, O. Khayam, N. Modi, M. R. Chitgarha, P. Mertz, W. Ko, R. Maher, J. Osenbach, J. T. Rahn, H. Sun, K.-T. Wu, M. Mitchell, and D. Welch, "System-on-Chip Photonic Integrated Circuits," *IEEE Journal of Selected Topics in Quantum Electronics*, vol. 24, no. 1, pp. 1–20, 2018, ISSN: 21910359. DOI: 10.1109/JSTQE.2017.2717863.

[7] V. Lal, J. Summers, N. Kim, S. W. Corzine, P. Evans, M. Lauermann, A. Nguyen, A. Hosseini, M. Lu, J. T. Rahn, M. R. Chitgarha, J. Zhang, J. Osenbach, T. Vallaitis, P. Samra, C. Park, M. Kuntz, J. Tang, C. Tsai, H. Sun, R. Schmogrow, D. Pavinski, B. Behnia, P. Mertz, T. Butrie, K. T. Wu, M. Mitchell, M. Ziari, M. Reffle, D. Welch, and F. Kish, "Extended C-Band Tunable Multi-Channel InP-Based Coherent Transmitter PICs," *Journal of Lightwave Technology*, vol. 35, no. 7, pp. 1320–1327, 2017, ISSN: 07338724. DOI: 10.1109/JLT.2017.2670547.

[8] T. Komljenovic, M. Davenport, J. Hulme, A. Y. Liu, C. T. Santis, A. Spott, S. Srinivasan, E. J. Stanton, C. Zhang, and J. E. Bowers, "Heterogeneous silicon photonic integrated circuits," *Journal of Lightwave Technology*, vol. 34, no. 1, pp. 20–35, 2016, ISSN: 07338724. DOI: 10.1109/JLT.2015.2465382.

[9] T. Y. Fan, "Laser beam combining for high-power, high-radiance sources," *IEEE Journal on Selected Topics in Quantum Electronics*, vol. 11, no. 3, pp. 567–577, May 2005, ISSN: 1077260X. DOI: 10.1109/JSTQE.2005.850241.

[10] A. Brignon, Ed., *Coherent Laser Beam Combining*. Weinheim, Germany: Wiley-VCH, Sep. 2013, pp. 1–481, ISBN: 9783527652778. DOI: 10.1002/9783527652778. [Online]. Available: http://doi.wiley.com/10.1002/9783527652778.

[11] A. Pasquazi, M. Peccianti, L. Razzari, D. J. Moss, S. Coen, M. Erkintalo, Y. K. Chembo, T. Hansson, S. Wabnitz, P. Del'Haye, X. Xue, A. M. Weiner, and R. Morandotti, *Micro-combs: A novel generation of optical sources*, Jan. 2018. DOI: 10.1016/j.physrep.2017.08.004.

[12] A. L. Gaeta, M. Lipson, and T. J. Kippenberg, "Photonic-chip-based frequency combs," *Nature Photonics*, vol. 13, no. 3, pp. 158–169, Mar. 2019, ISSN: 17494893. DOI: 10.1038/s41566-019-0358-x. [Online]. Available: https://doi.org/10.1038/s41566-019-0358-x.

[13] J. Ye and S. T. Cundiff, Eds., *Femtosecond Optical Frequency Comb: Principle, Operation, and Applications*. New York, NY: Springer, 2005, pp. 1–361. DOI: 10.1007/b102450.

[14] P. Del'Haye, A. Schliesser, O. Arcizet, T. Wilken, R. Holzwarth, and T. J. Kippenberg, "Optical frequency comb generation from a monolithic microresonator," *Nature*, vol. 450, no. 7173, pp. 1214–1217, Dec. 2007, ISSN: 14764687. DOI: 10.1038/nature06401. [Online]. Available: https://www.nature.com/articles/nature06401.

[15] B. Stern, X. Ji, Y. Okawachi, A. L. Gaeta, and M. Lipson, "Battery-operated integrated frequency comb generator," *Nature*, vol. 562, no. 7727, pp. 401–405, 2018, ISSN: 14764687. DOI: 10.1038/s41586-018-0598-9.

[16] A. S. Raja, A. S. Voloshin, H. Guo, S. E. Agafonova, J. Liu, A. S. Gorodnitskiy, M. Karpov, N. G. Pavlov, E. Lucas, R. R. Galiev, A. E. Shitikov, J. D. Jost, M. L. Gorodetsky, and T. J. Kippenberg, "Electrically pumped photonic integrated soliton microcomb," *Nature Communications*, vol. 10, no. 1, pp. 1–8, Dec. 2019, ISSN: 20411723. DOI: 10.1038/s41467-019-08498-2. [Online]. Available: https://doi.org/10.1038/s41467-019-08498-2.

[17] B. Shen, L. Chang, J. Liu, H. Wang, Q.-F. Yang, C. Xiang, R. N. Wang, J. He, T. Liu, W. Xie, J. Guo, D. Kinghorn, L. Wu, Q. X. Ji, T. J. Kippenberg, K. Vahala, and J. E. Bowers, "Integrated turnkey soliton microcombs," *Nature*, vol. 582, no. 7812, pp. 365–369, Jun. 2020, ISSN: 14764687. DOI: 10.1038/s41586-020-2358-x. [Online]. Available: https://doi.org/10.1038/s41586-020-2358-x.

[18] X. Xue, Y. Xuan, Y. Liu, P.-H. Wang, S. Chen, J. Wang, D. E. Leaird, M. Qi, and A. M. Weiner, "Mode-locked dark pulse Kerr combs in normal-dispersion microresonators," *Nature Photonics*, vol. 9, no. 9, pp. 594–600, Aug. 2015, ISSN: 1749-4885, 1749-4893. DOI: 10.1038/nphoton.2015.137. [Online]. Available: http://www.nature.com/doifinder/10.1038/nphoton.2015.137%20http://www.nature.com/nphoton/journal/v9/n9/pdf/nphoton.2015.137.pdf.

[19] X. Xue, P.-H. Wang, Y. Xuan, M. Qi, and A. M. Weiner, "Microresonator Kerr frequency combs with high conversion efficiency," *Laser & Photonics Reviews*, vol. 11, no. 1, p. 1 600 276, Jan. 2017, ISSN: 18638880. DOI: 10.1002/lpor.201600276. [Online]. Available: http://doi.wiley.com/10.1002/lpor.201600276.

[20] M. S. Alshaykh, J. D. McKinney, and A. M. Weiner, "Radio-Frequency Signal Processing Using Optical Frequency Combs," *IEEE Photonics Technology Letters*, vol. 31, no. 23, pp. 1874–1877, Dec. 2019, ISSN: 19410174. DOI: 10.1109/LPT.2019.2946542.

[21] P. Marin-Palomo, J. N. Kemal, M. Karpov, A. Kordts, J. Pfeifle, M. H. Pfeiffer, P. Trocha, S. Wolf, V. Brasch, M. H. Anderson, R. Rosenberger, K. Vijayan, W. Freude, T. J. Kippenberg, and C. Koos, "Microresonator-based solitons for massively parallel coherent optical communications," *Nature*, vol. 546, no. 7657, pp. 274–279, Jun. 2017, ISSN: 14764687. DOI: 10.1038/nature22387. [Online]. Available: https://www.nature.com/articles/nature22387.

[22] A. Fülöp, M. Mazur, A. Lorences-Riesgo, Ó. B. Helgason, P.-H. Wang, Y. Xuan, D. E. Leaird, M. Qi, P. A. Andrekson, A. M. Weiner, and V. Torres-Company, "High-order coherent communications using mode-locked dark-pulse Kerr combs from microresonators," *Nature Communications*, vol. 9, no. 1, pp. 1–8, Dec. 2018, ISSN: 20411723. DOI: 10.1038/s41467-018-04046-6. [Online]. Available: www.nature.com/naturecommunications.

[23] A. J. Metcalf, V. Torres-Company, D. E. Leaird, and A. M. Weiner, "High-power broadly tunable electrooptic frequency comb generator," *IEEE Journal on Selected Topics in Quantum Electronics*, vol. 19, no. 6, pp. 231–236, 2013, ISSN: 1077260X. DOI: 10.1109/JSTQE.2013.2268384.

[24] N. Andriolli, T. Cassese, M. Chiesa, C. De Dios, and G. Contestabile, "Photonic integrated fully tunable comb generator cascading optical modulators," *Journal of Lightwave Technology*, vol. 36, no. 23, pp. 5685–5689, Dec. 2018, ISSN: 07338724. DOI: 10.1109/JLT.2018.2877020.

[25] M. Zhang, B. Buscaino, C. Wang, A. Shams-Ansari, C. Reimer, R. Zhu, J. M. Kahn, and M. Lončar, "Broadband electro-optic frequency comb generation in a lithium niobate microring resonator," *Nature*, vol. 568, no. 7752, pp. 373–377, Apr. 2019, ISSN: 14764687. DOI: 10.1038/s41586-019-1008-7. [Online]. Available: https://doi.org/10.1038/s41586-019-1008-7.

[26] N. Li, Purnawirman, Z. Su, E. S. Magden, P. T. Callahan, K. Shtyrkova, M. Xin, A. Ruocco, C. Baiocco, E. P. Ippen, F. X. Kärtner, J. D. B. Bradley, D. Vermeulen, and M. R. Watts, "High-power thulium lasers on a silicon photonics platform," *Optics Letters*, vol. 42, no. 6, pp. 1181–1184, 2017, ISSN: 0146-9592. DOI: 10.1364/ol.42.001181.

[27] M. A. Tran, D. Huang, and J. E. Bowers, "Tutorial on narrow linewidth tunable semiconductor lasers using Si/III-V heterogeneous integration," *APL Photonics*, vol. 4, no. 11, p. 111 101, Nov. 2019, ISSN: 23780967. DOI: 10.1063/1.5124254.

[28] B. Stern, X. Ji, A. Dutt, and M. Lipson, "Compact narrow-linewidth integrated laser based on low-loss silicon nitride ring resonator," *Optics Letters*, vol. 42, no. 21, pp. 4541–4544, Aug. 2017, ISSN: 0146-9592. DOI: 10.1364/ol.42.004541. [Online]. Available: https://www.osapublishing.org/viewmedia.cfm?uri=ol-42-21-4541&seq=0&html=true%20https://www.osapublishing.org/abstract.cfm?uri=ol-42-21-4541%20https://www.osapublishing.org/ol/abstract.cfm?uri=ol-42-21-4541.

[29] N. Kobayashi, K. Sato, M. Namiwaka, K. Yamamoto, S. Watanabe, T. Kita, H. Yamada, and H. Yamazaki, "Silicon Photonic Hybrid Ring-Filter External Cavity Wavelength Tunable Lasers," *Journal of Lightwave Technology*, vol. 33, no. 6, pp. 1241–1246, Mar. 2015.

[30] D. F. Welch and D. G. Mehuys, "High-power coherent, semiconductor laser, master oscillator power amplifiers and amplifier arrays," in *Diode Laser Arrays*, D. Botez and D. R. Scifres, Eds., New York, NY: Cambridge University, 1994, ch. 2, pp. 72–122, ISBN: 0521419751. DOI: 10.1017/cbo9780511524127.003.

[31] L. Hou and J. H. Marsh, "1.55-μm distributed feedback laser monolithically integrated with amplifier array," *Optics Letters*, vol. 40, no. 2, pp. 213–216, Jan. 2015, ISSN: 0146-9592. DOI: 10.1364/ol.40.000213.

[32] J. C. Hulme, J. K. Doylend, M. J. R. Heck, J. D. Peters, M. L. Davenport, J. T. Bovington, L. A. Coldren, and J. E. Bowers, "Fully integrated hybrid silicon two dimensional beam scanner," *Optics Express*, vol. 23, no. 5, pp. 5861–5874, Mar. 2015, ISSN: 1094-4087. DOI: 10.1364/oe.23.005861.

[33] Y. Zhu and L. Zhu, "Integrated single frequency, high power laser sources based on monolithic and hybrid coherent beam combining," *IEEE Journal of Selected Topics in Quantum Electronics*, vol. 24, no. 6, pp. 1–8, Nov. 2018, ISSN: 21910359. DOI: 10.1109/JSTQE.2018.2836976.

[34] K. Morito and S. Tanaka, "Record high saturation power (+22 dBm) and low noise figure (5.7 dB) polarization-insensitive SOA module," *IEEE Photonics Technology Letters*, vol. 17, no. 6, pp. 1298–1300, Jun. 2005, ISSN: 10411135. DOI: 10.1109/LPT.2005.846472.

[35] X. J. Leijtens, B. Kuhlow, and M. K. Smit, "Arrayed waveguide gratings," in *Springer Series in Optical Sciences*, vol. 123, Berlin, Heidelberg: Springer, 2006, pp. 125–187, ISBN: 3540317694. DOI: 10.1007/3-540-31770-8{_}5. [Online]. Available: https://link.springer.com/chapter/10.1007/3-540-31770-8_5.

[36] Q. Cheng, M. Bahadori, M. Glick, S. Rumley, and K. Bergman, "Recent advances in optical technologies for data centers: a review," *Optica*, vol. 5, no. 11, p. 1354, Nov. 2018, ISSN: 2334-2536. DOI: 10.1364/optica.5.001354. [Online]. Available: https://doi.org/10.1364/OPTICA.5.001354.

[37] A. Hosseini, M. Lu, R. Going, P. Samra, S. Amiralizadeh, A. Nguyen, J. Rahn, V. Dominic, A. Awadalla, S. Corzine, N. Kim, J. Summers, D. Gold, J. Tang, H.-S. Tsai, K. Weidner, P. Abolghasem, M. Lauermann, J. Zhang, J. Yan, T. Vallaitis, G. Gilardi, A. Dentai, N. Modi, P. Evans, V. Lal, M. Kuntz, D. Pavinski, M. Ziari, J. Osenbach, M. Missey, A. James, T. Butrie, H. Sun, K.-T. Wu, M. Mitchell, M. Reffle, D. Welch, and F. Kish, "Extended C-band tunable multi-channel InP-based coherent receiver PICs," *Optics Express*, vol. 25, no. 16, p. 18 853, Aug. 2017, ISSN: 1094-4087. DOI: 10.1364/oe.25.018853. [Online]. Available: https://doi.org/10.1364/OE.25.018853.

[38] P. Minzioni, C. Lacava, T. Tanabe, J. Dong, X. Hu, G. Csaba, W. Porod, G. Singh, A. E. Willner, A. Almaiman, V. Torres-Company, J. Schröder, A. C. Peacock, M. J. Strain, F. Parmigiani, G. Contestabile, D. Marpaung, Z. Liu, J. E. Bowers, L. Chang, S. Fabbri, M. Ramos Vázquez, V. Bharadwaj, S. M. Eaton, P. Lodahl, X. Zhang, B. J. Eggleton, W. J. Munro, K. Nemoto, O. Morin, J. Laurat, and J. Nunn, "Roadmap on all-optical processing," *Journal of Optics (United Kingdom)*, vol. 21, no. 6, p. 063 001, May 2019, ISSN: 20408986. DOI: 10.1088/2040-8986/ab0e66. [Online]. Available: https://doi.org/10.1088/2040-8986/ab0e66.

[39] A. M. Weiner, "Ultrafast optical pulse shaping: A tutorial review," en, *Optics Communications*, vol. 284, no. 15, pp. 3669–3692, Jul. 2011, ISSN: 00304018. DOI: 10.1016/j.optcom.2011.03.084. [Online]. Available: http://linkinghub.elsevier.com/retrieve/pii/S0030401811003750%20http://ac.els-cdn.com/S0030401811003750/1-s2.0-S0030401811003750-main.pdf?_tid=3ea6c028-8499-11e5-92bc-00000aab0f02&acdnat=1446823122_9446bbebeda5830d6bdc3f2e87e63fc0.

[40] N. K. Fontaine, R. P. Scott, C. Yang, D. J. Geisler, J. P. Heritage, K. Okamoto, and S. J. Yoo, "Compact 10 GHz loopback arrayed-waveguide grating for high-fidelity optical arbitrary waveform generation," en, *Optics Letters*, vol. 33, no. 15, p. 1714, Aug. 2008, ISSN: 0146-9592, 1539-4794. DOI: 10.1364/OL.33.001714. [Online]. Available: https://www.osapublishing.org/ol/abstract.cfm?uri=ol-33-15-1714%20http://www.researchgate.net/profile/David_Geisler/publication/23140846_Compact_10_GHz_loopback_arrayed-waveguide_grating_for_high-fidelity_optical_arbitrary_waveform_generation/links/02e7e517.

[41] A. Metcalf, H.-J. Kim, D. Leaird, J. Jaramillo-Villegas, K. McKinzie, V. Lal, A. Hosseini, G. Hoefler, F. Kish, and A. Weiner, "Integrated line-by-line optical pulse shaper for high-fidelity and rapidly reconfigurable RF-filtering," *Optics Express*, vol. 24, no. 21, pp. 23 925–23 940, 2016, ISSN: 10944087. DOI: 10.1364/OE.24.023925.

[42] G. E. Hoefler, Y. Zhou, M. Anagnosti, A. Bhardwaj, P. Abolghasem, A. James, S. Luna, P. Debackere, A. Dentai, T. Vallaitis, P. Liu, M. Missey, S. Corzine, P. Evans, V. Lal, M. Ziari, D. Welch, F. Kish, J. S. Suelzer, P. S. Devgan, and N. G. Usechak, "Foundry Development of System-On-Chip InP-Based Photonic Integrated Circuits," *IEEE Journal of Selected Topics in Quantum Electronics*, vol. 25, no. 5, pp. 1–17, 2019, ISSN: 21910359. DOI: 10.1109/JSTQE.2019.2906270.

[43] J. W. Raring, E. J. Skogen, M. L. Mašanović, S. P. Denbaars, and L. A. Coldren, "Demonstration of high saturation power/high gain SOAs using quantum well intermixing based integration platform," *Electronics Letters*, vol. 41, no. 24, pp. 1345–1346, 2005, ISSN: 00135194. DOI: 10.1049/el:20053248.

[44] S. M. Redmond, K. J. Creedon, J. E. Kansky, S. J. Augst, L. J. Missaggia, M. K. Connors, R. K. Huang, B. Chann, T. Y. Fan, G. W. Turner, and A. Sanchez-Rubio, "Active coherent beam combining of diode lasers," *Optics Letters*, vol. 36, no. 6, pp. 999–1001, 2011, ISSN: 0146-9592. DOI: 10.1364/ol.36.000999.

[45] T. Motaweh, P. Morel, A. Sharaiha, R. Brenot, A. Verdier, and M. Guegan, "Wideband Gain MQW-SOA Modeling and Saturation Power Improvement in a Tri-Electrode Configuration," *Journal of Lightwave Technology*, vol. 35, no. 10, pp. 2003–2009, 2017, ISSN: 07338724. DOI: 10.1109/JLT.2017.2657821.

[46] R. W. Tkach and A. R. Chraplyvy, "Regimes of feedback effects in 1. 5-μm distributed feedback lasers," *Journal of Lightwave Technology*, vol. 4, no. 11, pp. 1655–1661, 1986, ISSN: 07338724. DOI: 10.1109/jlt.1986.1074666.

[47] S. Donati and R.-H. Horng, "The Diagram of Feedback Regimes Revisited," *IEEE Journal on Selected Topics in Quantum Electronics*, vol. 19, no. 4, 2013, ISSN: 1077260X. DOI: 10.1109/JSTQE.2012.2234445.

[48] M. A. Seldowitz, J. P. Allebach, and D. W. Sweeney, "Synthesis of digital holograms by direct binary search," *Applied Optics*, vol. 26, no. 14, pp. 2788–2798, 1987, ISSN: 0003-6935. DOI: 10.1364/ao.26.002788.

[49] M. S. Zediker, H. R. Appelman, B. G. Clay, J. R. Heidel, R. W. Herrick, J. M. Haake, J. W. Martinosky, F. Streumph, and R. A. Williams, "10-amplifier coherent array based on active-integrated optics," in *Laser Diode Technology and Applications II*, vol. 1219, 1990, pp. 197–210, ISBN: 0819402605. DOI: 10.1117/12.18257.

[50] T. Okoshi, K. Kikuchi, and A. Nakayama, "Novel method for high resolution measurement of laser output spectrum," *Electronics Letters*, vol. 16, no. 16, pp. 630–631, 1980, ISSN: 00135194. DOI: 10.1049/el:19800437.

[51] X. Chen, M. Han, Y. Zhu, B. Dong, and A. Wang, "Implementation of a loss-compensated recirculating delayed self-heterodyne interferometer for ultranarrow laser linewidth measurement," *Applied Optics*, vol. 45, no. 29, pp. 7712–7717, 2006, ISSN: 15394522. DOI: 10.1364/AO.45.007712.

[52] K. Kikuchi, "Effect of 1 /f-Type FM Noise on semiconductor laser linewidth residual in high-power limit," *IEEE Journal of Quantum Electronics*, vol. 25, no. 4, pp. 684–688, 1989, ISSN: 15581713. DOI: 10.1109/3.17331.

[53] T. N. Huynh, L. Nguyen, and L. P. Barry, "Delayed Self-Heterodyne Phase Noise Measurements with Coherent Phase Modulation Detection," *IEEE Photonics Technology Letters*, vol. 24, no. 4, pp. 249–251, 2012, ISSN: 10411135. DOI: 10.1109/LPT.2011.2174216.

[54] R. Nagarajan, D. Lambert, M. Kato, V. Lal, G. Goldfarb, J. Rahn, M. Kuntz, J. Pleumeekers, A. Dentai, H. S. Tsai, R. Malendevich, M. Missey, K.-T. Wu, H. Sun, J. McNicol, J. Tang, J. Zhang, T. Butrie, A. Nilsson, M. Reffle, F. Kish, and D. Welch, "10 channel, 100Gbit/s per channel, dual polarization, coherent QPSK, monolithic InP receiver photonic integrated circuit," in *Optical Fiber Communication Conference*, Optical Society of America, Mar. 2011, OML7, ISBN: 9781557529060. DOI: 10.1364/ofc.2011.oml7.

[55] L. B. Mercer, "1/f Frequency Noise Effects on Self-Heterodyne Linewidth Measurements," *Journal of Lightwave Technology*, vol. 9, no. 4, pp. 485–493, 1991, ISSN: 15582213. DOI: 10.1109/50.76663.

[56] B. K. A. Ngoi and K. Venkatakrishnan, "Techniques to eliminate error induced due to acousto-optic modulator vibration in heterodyne interferometry," *Optical Engineering*, vol. 38, no. 12, pp. 2050–2054, 1999, ISSN: 0091-3286. DOI: 10.1117/1.602310.

[57] M. W. Hamilton, "An introduction to stabilized lasers," *Contemporary Physics*, vol. 30, no. 1, pp. 21–33, 1989, ISSN: 13665812. DOI: 10.1080/00107518908222588.

[58] J. L. Hall, M. S. Taubman, and J. Ye, "LASER STABILIZATION: Quantifying Frequency Stability," in *Handbook of Optics: Volume IV - Fiber Optics and Nonlinear Optics*, M. Bass, J. M. Enoch, E. W. V. Stryland, and W. L. Wolfe, Eds., 2nd ed., McGraw-Hill, 1999, ch. 27.

[59] M. Chen, Z. Meng, J. Wang, and W. Chen, "Ultra-narrow linewidth measurement based on Voigt profile fitting," *Optics Express*, vol. 23, no. 5, pp. 6803–6808, Mar. 2015, ISSN: 1094-4087. DOI: 10.1364/oe.23.006803.

[60] K. Vahala and A. Yariv, "Semiclassical Theory of Noise in Semiconductor Lasers-Part II," *IEEE JOURNAL OF QUANTUM ELECTRONICS*, vol. 19, no. 6, pp. 1102–1109, 1983.

[61] G. Di Domenico, S. Schilt, and P. Thomann, "Simple approach to the relation between laser frequency noise and laser line shape," *Applied Optics*, vol. 49, no. 25, pp. 4801–4807, 2010, ISSN: 15394522. DOI: 10.1364/AO.49.004801.

[62] H. Ludvigsen, M. Tossavainen, and M. Kaivola, "Laser linewidth measurements using self-homodyne detection with short delay," *Optics Communications*, vol. 155, pp. 180–186, 1998, ISSN: 00304018. DOI: 10.1016/S0030-4018(98)00355-1.

[63] T. N. Huynh, L. Nguyen, and L. P. Barry, "Phase noise characterization of SGDBR lasers using phase modulation detection method with delayed self-heterodyne measurements," *Journal of Lightwave Technology*, vol. 31, no. 8, pp. 1300–1308, 2013, ISSN: 07338724. DOI: 10.1109/JLT.2013.2247564.

[64] C. Xiang, W. Jin, J. Guo, J. D. Peters, M. J. Kennedy, J. Selvidge, P. A. Morton, and J. E. Bowers, "Temperature stable, narrow linewidth heterogeneously integrated semiconductor laser with Si3N4 cavity," in *CLEO: Science and Innovations*, 2020, STu3M.6.

[65] S. D. Saliba and R. E. Scholten, "Linewidths below 100 kHz with external cavity diode lasers," *Applied Optics*, vol. 48, no. 36, pp. 6961–6966, Dec. 2009, ISSN: 15394522. DOI: 10.1364/AO.48.006961. [Online]. Available: https://www.osapublishing.org/viewmedia.cfm?uri=ao-48-36-6961&seq=0&html=true%20https://www.osapublishing.org/abstract.cfm?uri=ao-48-36-6961%20https://www.osapublishing.org/ao/abstract.cfm?uri=ao-48-36-6961.

[66] W. P. Robins, *Phase Noise in Signal Sources*, J. E. Flood and C. J. Hughes, Eds. London: The Institution of Engineering and Technology, Jan. 1982, pp. 1–336. DOI: 10.1049/pbte009e. [Online]. Available: https://digital-library.theiet.org/content/books/te/pbte009e.

[67] W. Kester, *Understand SINAD, ENOB, SNR, THD, THD + N, and SFDR so You Don't Get Lost in the Noise Floor*, 2009. [Online]. Available: https://www.analog.com/media/en/training-seminars/tutorials/MT-003.pdf.

[68] K.-J. Boller, A. van Rees, Y. Fan, J. Mak, R. E. M. Lammerink, C. A. A. Franken, P. J. M. van der Slot, D. A. I. Marpaung, C. Fallnich, J. P. Epping, R. M. Oldenbeuving, D. Geskus, R. Dekker, I. Visscher, R. Grootjans, C. G. H. Roeloffzen, M. Hoekman, E. J. Klein, A. Leinse, and R. G. Heideman, "Hybrid Integrated Semiconductor Lasers with Silicon Nitride Feedback Circuits," *Photonics*, vol. 7, no. 4, pp. 1–33, Dec. 2019, ISSN: 2304-6732. DOI: 10.3390/photonics7010004. [Online]. Available: https://www.mdpi.com/2304-6732/7/1/4.

[69] W. Liang, V. S. Ilchenko, A. A. Savchenkov, A. B. Matsko, D. Seidel, and L. Maleki, "Whispering-gallery-mode-resonator-based ultranarrow linewidth external-cavity semiconductor laser," *Optics Letters*, vol. 35, no. 16, pp. 2822–2824, Aug. 2010, ISSN: 0146-9592. DOI: 10.1364/ol.35.002822.

[70] V. S. Ilchenko, E. Dale, W. Liang, J. Byrd, D. Eliyahu, A. A. Savchenkov, A. B. Matsko, D. Seidel, and L. Maleki, "Compact tunable kHz-linewidth semiconductor laser stabilized with a whispering-gallery mode microresonator," in *Proc. SPIE*, vol. 7913, 2011, 1G–1.

[71] A. Gil-Molina, O. Westreich, Y. Antman, X. Ji, A. L. Gaeta, and M. Lipson, "Robust Hybrid III-V/Si 3 N 4 Laser with kHz-Linewidth and GHz-Pulling Range," in *2020 Conference on Lasers and Electro-Optics (CLEO)*, 2020, pp. 1–2.

[72] Y. I. Xuan, Y. Liu, L. T. Varghese, A. J. Metcalf, X. Xue, P.-H. Wang, K. Han, J. A. Jaramillo-Villegas, A. A. Noman, C. Wang, S. Kim, M. Teng, Y. J. Lee, B. Niu, L. I. Fan, J. Wang, D. E. Leaird, A. M. Weiner, and M. Qi, "High-Q silicon nitride microresonators exhibiting low-power frequency comb initiation," *Optica*, vol. 3, no. 11, pp. 1171–1180, 2016. DOI: 10.1364/OPTICA.3.001171. [Online]. Available: http://dx.doi.org/10.1364/OPTICA.3.001171.

[73] K. A. McKinzie, D. E. Leaird, D. Mathine, M. Anagnosti, G. E. Hoefler, Z. Kong, C. Bao, V. Lal, A. Hosseini, F. Kish, and A. M. Weiner, "InP integrated pulse shaper with 48 channel, 50 GHz spacing amplitude and phase control," in *30th Annual Conference of the IEEE Photonics Society, IPC 2017*, vol. 2017-January, Institute of Electrical and Electronics Engineers Inc., Nov. 2017, pp. 197–198, ISBN: 9781509065783. DOI: 10.1109/IPCon.2017.8116067.

[74] A. J. Metcalf, V. Torres-Company, D. E. Leaird, and A. M. Weiner, "High-power broadly tunable electrooptic frequency comb generator," *IEEE Journal on Selected Topics in Quantum Electronics*, vol. 19, no. 6, pp. 231–236, 2013, ISSN: 1077260X. DOI: 10.1109/JSTQE.2013.2268384.

[75] F. Ferdous, D. E. Leaird, C.-B. Huang, and A. M. Weiner, "Dual-comb electric-field cross-correlation technique for optical arbitrary waveform characterization," *Optics Letters*, vol. 34, no. 24, p. 3875, Dec. 2009, ISSN: 0146-9592. DOI: 10.1364/ol.34.003875. [Online]. Available: https://www.osapublishing.org/viewmedia.cfm?uri=ol-34-24-3875&seq=0&html=true%20https://www.osapublishing.org/abstract.cfm?uri=ol-34-24-3875%20https://www.osapublishing.org/ol/abstract.cfm?uri=ol-34-24-3875.

[76] V. R. Supradeepa, C. M. Long, D. E. Leaird, and A. M. Weiner, "Self-referenced characterization of optical frequency combs and arbitrary waveforms using a simple, linear, zero-delay implementation of spectral shearing interferometry," *Optics Express*, vol. 18, no. 17, p. 18 171, Aug. 2010, ISSN: 1094-4087. DOI: 10.1364/oe.18.018171. [Online]. Available: http://www.aragonphotonics.com/ficha.php?cat=76&id=80&opt=2.